



Molecular cartography of the human down syndrome and trisomic mouse brain

Received: 1 November 2024

Accepted: 27 August 2025

Published online: 30 September 2025

Check for updates

Min Yi Feng ^{1,2}, Wuxinhao Cao ^{1,3,4,5}, Nareh Tahmasian ¹, Bharti Kukreja ¹, Gen Li ^{1,6}, Bianca Rusu ^{1,2}, Ji-Young Youn ^{2,7} & Brian T. Kalish ^{1,2,8,9,10}

Down syndrome (DS, or Trisomy 21) is one of the most common genetic causes of intellectual disability. DS results in both abnormal neurodevelopment and accelerated neurodegeneration, but the molecular mechanisms underlying abnormal corticogenesis are incompletely understood. To gain molecular insight into the prenatal neurobiology of DS, we performed single-nucleus sequencing, spatial transcriptomics, and proteomics on mid-gestational prenatal human cortex. We captured altered expression dynamics of lineage commitment genes and de-repression of transposable elements in DS neural progenitor cells, which suggest changes to the fate and functionality of neuronal and glial cells. Given the importance of linking human and model system pathobiology, we also performed highly multiplexed RNA in situ spatial transcriptomics on a well-established trisomic mouse model (Ts65Dn) to study the cellular landscape of the trisomic brain during early development and maturation. We profiled the spatial transcriptome of > 240,000 cells in the mouse brain and identified trisomy-associated gene expression patterns in the molecular control of neurogenesis and gliogenesis. Together, our study provides an extensive resource for understanding of the complex multicellular processes underlying DS neurodevelopment.

Down syndrome (DS) is the most common chromosomal cause of intellectual disability worldwide, affecting roughly 1 in 700 live births¹. DS is caused by the presence of an extra copy or major portion of human chromosome 21 (Hsa21) that produces a genetic imbalance. DS is associated with disrupted neurodevelopment leading to lifelong learning, memory, and language impairment, as well as early-onset dementia^{1,2}. The phenotypic features of the DS brain originate during prenatal life^{3,4}, during which there is marked reduction in neural progenitor cell (NPC) proliferation, differentiation, and migration^{5,6}, corresponding to reduced cortical volume during late gestation⁷. Additionally, DS is marked by an augmented switch of NPCs towards a

gliogenic fate⁸. Impaired differentiation within the oligodendrocyte lineage⁹, accompanied with astrogliosis¹⁰, contributes to white matter abnormalities observed in young children with DS^{11,12}. However, there is a limited understanding of how the abnormal genomic landscape in DS disrupts specific intrauterine neurodevelopmental processes, leading to cortical dysmaturation.

To address this gap, we employed an integrated multi-omics approach using single-nucleus (sn)RNA-sequencing, high-resolution spatial transcriptomics (Slide-seq)¹³, and proteomics to characterize the cellular phenotypes and spatial architecture of the mid-gestation human DS brain. Of note, Slide-seq is a whole-transcriptional spatial

¹Program in Neuroscience and Mental Health, SickKids Research Institute, Toronto, ON M5G 1L7, Canada. ²Department of Molecular Genetics, University of Toronto, Toronto, ON M5G 1A8, Canada. ³Department of Biochemistry, University of Toronto, Toronto, ON M5G 1A8, Canada. ⁴Department of Statistical Science, University of Toronto, Toronto, ON M5G 1A8, Canada. ⁵Department of Immunology, University of Toronto, Toronto, ON M5G 1A8, Canada. ⁶Department of Cell and System Biology, University of Toronto, Toronto, ON M5G 1A8, Canada. ⁷Program in Molecular Medicine, SickKids Research Institute, Toronto, ON M5G 1L7, Canada. ⁸Division of Neonatology, Department of Paediatrics, Hospital for Sick Children, Toronto, ON M5G 1L7, Canada. ⁹Division of Newborn Medicine, Department of Pediatrics, Boston Children's Hospital, Boston, MA 02115, USA. ¹⁰F.M. Kirby Neurobiology Center, Boston Children's Hospital, Boston, MA 02115, USA. e-mail: brian.kalish@childrens.harvard.edu

approach in which RNA from tissue sections is transferred onto a surface covered in DNA-barcoded beads with known positions, allowing the locations of the RNA to be inferred by sequencing¹³. We found significant changes in pathways that regulate transcriptional and translational machinery, DNA repair, neural migration, chromatin remodeling, and in the developmental progression of NPCs to mature neurons. Importantly, given the notable changes in chromatin-modifying molecules, we identified cell-type-specific activation of transposable elements (TEs) in the developing human DS brain.

To build upon our human data, we used the Ts65Dn mouse model of DS, a widely used system for testing potential therapeutics and investigating novel pathomechanisms¹. We performed imaging-based spatial transcriptomics (multiplexed error-robust fluorescence in situ hybridization; MERFISH) in the Ts65Dn mouse model at two critical time points: postnatal day 0 (PO) and 6 months (6mo)^{14,15}. MERFISH is a massively parallel single-molecule imaging approach that enables measurement of copy number and spatial position of hundreds of unique gene transcripts. Consistent with our prenatal human dataset, we identified dysregulation of genes involved in transcriptional and post-transcriptional gene regulation, as well as NPC maintenance, proliferation, and migration. Using computational tools to quantify changes to the cellular microenvironment, we identified region- and age-specific alterations in the spatial relationship between neuronal and glial cell populations in the trisomic mouse brain.

Together, our cross-species dataset represents a rich resource for understanding the prenatal origins and trajectory of brain disorganization in human DS and Ts65Dn mice, nominating molecular pathways that may lead to impaired lineage specification and function. Our dataset of gene expression changes in the developing human DS brain and trisomic mouse brain is accessible via our accompanying web interface (<https://neurodevelopment.shinyapps.io/Downsyndrome/>).

Results

Combined spatial and single-nucleus analysis of the prenatal human DS brain

We performed snRNA-seq (10x Genomics) on prenatal human brain samples spanning the second trimester of gestation (Fig. 1a). Detailed information of the tissue used is presented in Supplementary Data 1. Following stringent quality control filtering, doublet removal, and batch effect correction, we profiled 122,663 nuclei from the prenatal human brain (13–19 post-conception weeks (PCW); $n=5$ DS, $n=5$ euploid). After graph-based clustering, cell identities were assigned based on canonical marker gene expression and automated label transfer from published prenatal human brain data¹⁶: NPCs (including radial glia (RG), cycling (CP), and intermediate progenitors (IP)) expressing *SOX2*, *PAX6*, *EOMES*, *DLX1*, or *MKI67*; excitatory neurons (ExN) expressing *MEF2C*, *CUX2*, or *TLE4*; inhibitory neurons (InN) expressing *GAD1*, *PROX1*, *CNR1*, *SST*, *NPY*, or *LHX6*; striatal neurons (InN Striatum) expressing *CNTNS*, *ZFHXB3*, and *NGEF*; astrocyte progenitors expressing *SOX2*, *SPARC1L*, *SLC1A3*, and *GFAP*; oligodendrocyte progenitor cells (OPC) expressing *SOX2*, *PDGFRA*, *SOX10*, and *OLIG1*; oligodendrocytes expressing *MBP*, *SOX10*, and *OLIG1*; microglia expressing *ITGAM* and *CSF1R*; and vasculature-associated cells expressing *PDGFRB*, *RGSS*, *PECAMI*, and *ESAM* (Fig. 1b, c). The number of expressed genes and transcripts per nucleus were consistent across all samples, yielding a median of 1595 genes and 2399 transcripts per nucleus (Supplementary Fig. 1a).

Broad cell type populations were re-clustered separately to define intra-lineage heterogeneity and a complete taxonomy of the prenatal human brain. We identified five subtypes of NPCs, including outer RG (oRG) expressing *TNC*, *LIFR*, and *HOPX*¹⁷; ventricular RG (vRG) expressing *CRYAB* and *FBXO32*¹⁸; CP expressing *MKI67*, *TOP2A*, and *PPP1R17*; IP fated to an excitatory lineage expressing *EOMES*, *SSTR2*, and *PPP1R17*^{19,20}; and IP fated to an inhibitory lineage (IP IN) expressing

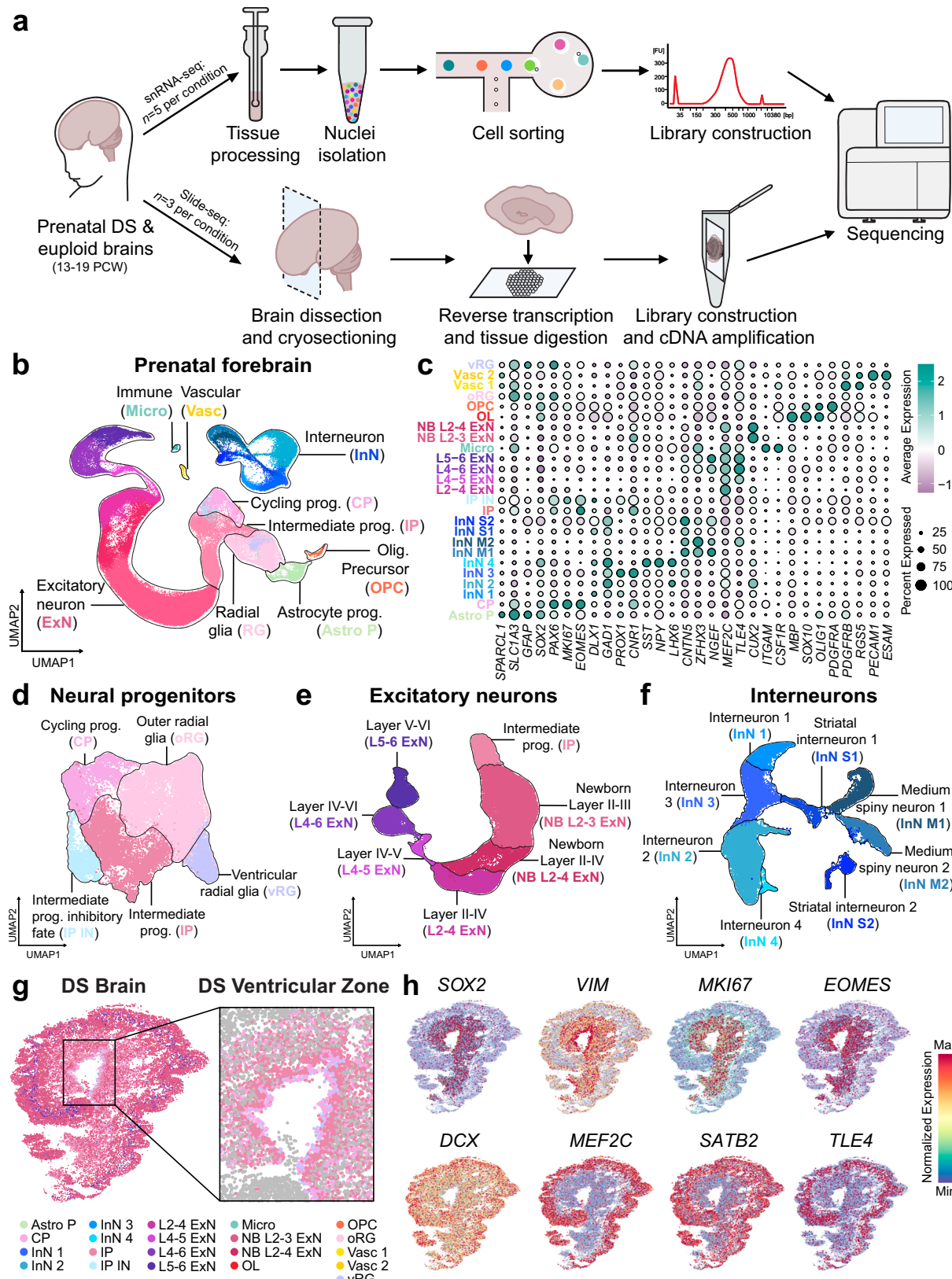
MKI67, *DLX1/2*, *GAD2*, *EOMES*, *TOP2A*, and *PPP1R17*^{20,21} (Fig. 1c, d; Supplementary Fig. 1b). We found six subtypes of cortical layer and/or development-specific ExN, including layer 5–6 ExN (LV-VI ExN) expressing *IL1RAPL2*, *TLE4*, *HS3ST4*, and *ARHGEF28*^{22,23}; layer 4–6 ExN (LIV-VI ExN) expressing *FOXP2*, *RORB*, *HS3ST4*, *TLE4*, and *SSTR2*; layer 4–5 ExN (LIV-V ExN) expressing *RORB*, *HS3ST4*, *TLE4*, and *SSTR2*; layer 2–4 ExN (LII–IV ExN) expressing *MEF2C* and *RORB*^{24,25}; newborn layers 2–4 ExN (NB LII–IV ExN) expressing *CUX2*, *RORB*, *PRSS12*, and the migratory markers *UNCSD* and *DCC*^{19,26,27}; and newborn layer 2–3 ExN (NB LII–III ExN) expressing *SLC17A6*, *CUX2*, and *PRSS12*^{23,28}, in addition to migratory markers (Fig. 1c, e; Supplementary Fig. 1b). We identified four subtypes of cortical InN and four subtypes of InN Striatum, including: general InN (InN 1) moderately expressing *GAD1/2*, *PROX1*, and *CALB2*; *GAD1/2* and *LHX6*-expressing InN (InN 2); *GAD1/2*, *PROX1*, *CNR1*, and *CALB2*-expressing InN (InN 3); *GAD1*, *SST*, *NPY*, and *LHX6*-expressing InN (InN 4); general InN Striatum (InN S1) expressing *FOXP2*, *IL1RAPL2*, and *GAD1/GAD2*; InN Striatum expressing *MEIS2*, *RELN*, and *GAD1/2* (InN S2); InN Striatum likely representing the D1-type medium spiny neuron (MSN) population (InN M1) expressing *MEIS2*, *EBFI*, *RELN*, *FOXP1*, and *FOXP2*, and lacking cortical InN markers^{29–32}; as well as InN Striatum likely representing the D2-type MSN population (InN M2) expressing *MEIS2*, *DRD2* and *FOXP1* and lacking cortical InN markers^{30,31,33,34} (Fig. 1c, f; Supplementary Fig. 1b). Granular cell typing of vascular and glia cells are described in the Methods. We did not find changes in cellular proportions between prenatal DS and euploid brains, which is consistent with recent literature³⁵ (Supplementary Fig. 1c).

To complement the droplet-based snRNA-seq dataset, we employed Slide-seqV2 (Curio Bioscience), a near-single cell resolution spatial transcriptomics approach¹³, to map diverse cell types in the prenatal human DS cortex and ventricular zone. We profiled tissue samples from 14–18 PCW ($n=3$ DS, $n=3$ euploid; Supplementary Data 1). Following library preparation, alignment, and stringent QC filtering (Supplementary Fig. 1d; Methods), we used our snRNA-seq dataset to confidently deconvolute expression data from each spatial pixel into cell type signatures³⁶ (Fig. 1g). Spatial mapping of NPCs and cortical layer markers revealed cell type annotations true to their spatial location in the ventricular zone ($n=14,490$) and neocortex ($n=159,508$) (Fig. 1h).

Differential gene expression analysis in the prenatal human DS brain

The triplication of Hsa21, which encodes approximately 230 protein-coding genes and 380 noncoding genes¹, leads to gene dosage imbalances that are believed to contribute to the phenotypic characteristics of DS^{37,38}. In line with previous studies^{39,40}, we identified notable cell type-specific transcriptional effects of Hsa21 triplication on genes within the DS critical region (DSCR) (Supplementary Fig. 2a). However, the magnitude and specificity of this overexpression varied by cell subtype, suggesting that certain cellular contexts may be differentially affected by Hsa21 triplication. To investigate the gene dosage effects during prenatal DS brain development, we performed differential gene expression (DGE) analysis between all DS and euploid cell subtypes from the snRNA-seq dataset, incorporating donor replicate as a covariate to control for inter-sample variability⁴¹. All DGE results are provided in Supplementary Data 2. Pathway analysis using the Gene Ontology (GO)^{42,43} and Reactome⁴⁴ databases revealed several key themes of mis-regulated gene expression during prenatal human DS brain development, which are summarized in Supplementary Data 3.

Several overarching themes of gene expression dysregulation emerged across most major cell types in the prenatal DS brain. One of the most prominent was the consistent downregulation of cell cycle-related pathways. This pattern was evident in the negative enrichment of multiple Reactome terms, including cell cycle and its regulation, M-



phase, S-phase, DNA synthesis and replication, and sister chromatid separation (Fig. 2a; Supplementary Data 3). These disruptions involved a broad array of key regulatory genes, such as cyclins and cyclin-dependent kinases (e.g. *CDK1*, *CDK4*, *CCND2*, *CCNG1*) as well as checkpoint regulators (e.g. *CDKN1B*, *TP53*) (Supplementary Data 2). To validate transcriptional changes in *TP53*, we performed

immunofluorescence analysis of SOX2⁺ NPCs (Supplementary Fig. 2b), revealing significantly reduced TP53 protein levels in prenatal DS brains compared to euploid controls (p value = 0.006; Supplementary Fig. 2c).

We also observed widespread dysregulation of post-transcriptional machinery in the DS prenatal brain. Multiple GO

Fig. 1 | Cellular characterization of the prenatal Down syndrome and euploid brain. **a** Schematic overview of the multi-omics approach utilizing single-nucleus (sn)RNA-seq and Slide-seq. **b** Uniform Manifold Approximation and Projection (UMAP) representation of all high-quality nuclei identified by snRNA-seq ($n = 122,663$). Each dot represents a nucleus. Cell type identity is delineated by the solid line. **c** Dotplot showing gene expression of canonical cell type markers used for cell type identification. Dot color represents normalized gene expression and dot diameter represents the proportion of nuclei expressing the gene. **d–f** UMAP representation of granular cell subtypes of **d**, neural progenitors, **e**, excitatory

neurons, and **f**, interneurons. Nuclei are color-coded by their cell subtype identity. **g** Spatial representation of a representative Down syndrome (DS) brain and a magnified view of the ventricular zone, captured by Slide-seq. Each dot represents the cell type with the highest proportional representation on a given bead. Only neural progenitor cells (NPCs) are colored in the ventricular zone. **h** Spatial plots of genes used to delineate the ventricular zone and neocortex, including *SOX2*, *VIM*, *MKI67*, *EOMES*, *DCX*, *MEF2C*, *SATB2*, and *TLE4*. Dot color represents normalized gene expression from the 10th to 90th percentiles.

biological processes including cytoplasmic translation, ribosome biogenesis and assembly, amide and peptide biosynthesis, and protein folding were negatively enriched (Fig. 2b), as were Reactome pathways related to translation initiation, elongation, and rRNA processing (Supplementary Data 3). This transcriptional signature encompassed reduced expression of translation initiation factors (e.g. *EIF3F*, *EIF3G*), elongation factors (e.g. *EEF1A1*, *EEF2*), and numerous ribosomal proteins (e.g. *RPL* and *RPS* gene families) (Supplementary Data 2). Autophagy also emerged as a significantly downregulated process (Fig. 2a). This included core components of the ATG8 family (e.g. *GABARAP*, *GABARAPL2*), chaperone-mediated autophagy proteins (e.g. *HSP90AA1*, *HSP90AB1*, *HSPA8*), and subunits of the Ragulator complex (e.g. *LAMTOR1*, *LAMTORS*) (Supplementary Data 2).

Immune-related pathways were similarly affected across several cell lineages. Both Reactome pathways involving innate and adaptive immune responses and GO terms related to immune regulation, viral life cycle, and cytokine production were negatively enriched (Fig. 2a, b). We identified reduced expression of several immune effectors, including damage-associated molecular patterns (e.g. *HMGB1/2/3*) and pro-inflammatory cytokine-like factors (e.g. *MIF*), as well as antigen presentation-associated genes (e.g. *HLA-A*) and ubiquitin-mediated signaling genes (*UBB/C*, *UBAS2*) (Supplementary Data 2).

Lastly, signaling through the SLIT-ROBO axis was notably impaired across several cell types. Reactome terms including ROBO receptor signaling and regulation of SLIT and ROBO expression, were negatively enriched (Fig. 2a), implicating this pathway in the disruption of cortical migration⁴⁵. Spatial transcriptomic analyses revealed reduced expression of *ROBO1* and *SLT1* in the DS cortex (Fig. 2c). This transcriptional reduction was supported by immunofluorescence staining (Fig. 2d), which demonstrated diminished ROBO1 protein levels in *NEUN*⁺ cortical neurons in prenatal human DS samples ($p = 0.017$; Fig. 2e). Given the role of ROBO1 in guiding NPC migration via SLIT chemorepellent signaling, these findings suggest that alterations in SLIT-ROBO signaling may contribute to impaired neuronal positioning in DS.

DS NPCs, including oRG, vRG, IP, and CP, showed cell-type-specific negative enrichment in pathways associated with neuronal differentiation. These pathways encompassed GO terms such as GABAergic, and forebrain neuron differentiation, as well as neuron fate commitment (Fig. 2b; Supplementary Data 3). Notably, we observed the downregulation of several key lineage-specification and differentiation-associated genes, including *ASCL1*, *SOX1/2/3*, *HESS*, *FOXO1*, and *BCL11B* (Fig. 2f–h). We also found a selective increase in the expression of immediate early genes (IEGs), *EGRI*, *FOS*, *JUN*, and *IER2* in DS NPCs, including RG, CP, and IP, but not in glial or mature neuron populations (Fig. 2f–h). Spatial plots from Slide-seq confirmed higher expression of IEGs in the prenatal DS brain (Supplementary Fig. 2d).

The expression of non-histone chromatin-associated proteins (e.g. *HMGB1/2*), polycomb-group proteins (e.g. *EZH2*, *EED*), chromatin modifiers (e.g. *KAT2A*, *AURKB*, *VRK1*), DNA methyltransferases (e.g. *DNMT1*, *DNMT3A*), histones (e.g. *H2AFZ/X/Y*), as well as histone deacetylases (e.g. *HDAC2/4*) were broadly downregulated in DS NPCs (Fig. 2f–h; Supplementary Data 2), as further illustrated in representative DS and euploid brains (Supplementary Fig. 2d). In contrast, chromatin regulators *USP16* and *DYRK1A* were upregulated, consistent

with their gene dosage increase in DS (Supplementary Fig. 2a). These widespread chromatin-related changes were accompanied by reduced expression of nuclear lamina-associated protein (*LMNB1*) (Fig. 2f–h). Together, these findings indicate changes in chromatin and nuclear architecture-related genes in DS NPCs, consistent with features previously associated with a senescence-like phenotype *in vitro*⁴⁶. To support these findings, we used immunofluorescence to quantify LMNB1 intensity in SOX2⁺ NPCs (Supplementary Fig. 2e), identifying a significant reduction of LMNB1 in DS relative to euploid brains (Supplementary Fig. 2f; p -value = 0.0001).

In GO analysis of ExN, we observed significant negative enrichment of interleukin family signaling pathways—particularly those involving IL-1, IL-4, IL-12, and IL-17—alongside downregulation of NOTCH and WNT signaling, and autophagy, based on Reactome analysis (Fig. 2a, b). Specifically, several immune effectors (e.g. *UBB/C*, *HMGB1/2*, *TRIM28*) and proteasome-associated genes (e.g. *PSMD4/78/I3* were downregulated in ExN populations (Fig. 3a, b; Supplementary Data 2). In contrast, InN showed positive enrichment of GO terms including synaptic signaling, regulation of synaptic plasticity, axon development, and cell-cell signaling (Fig. 2b). Notably, several genes associated with inhibitory synapse formation were upregulated, including GABA receptor subunits (e.g. *GABRB3*, *GABRG3*), as well as *MDGA2*, *NLGN1*, *NRG1*, *ERBB4*, *NTRK2/3*, and *CNTNS* broadly in InN populations (Fig. 3c, d). These findings add to the growing body of evidence suggesting that dysregulated GABAergic signaling and synaptic development may underlie core neurodevelopmental DS phenotypes^{47,48}.

Astrocyte progenitors demonstrated cell-type-specific GO processes, including microtubule-based transport and movement, cilium movement and organization, as well as cell projection assembly (Supplementary Data 3), as indicated by the upregulation of dynein-related genes (e.g. *DNAH14*, *DYNCII*), ciliary proteins (e.g. *CFAP161*) (Fig. 3e). These processes may be critical for astrocyte migration and positioning (Fig. 3e). GO analysis of microglia demonstrated positive enrichment of chromatin remodeling, alongside negative enrichment of cellular response to heat and cytokine production (Supplementary Data 3). Specifically, we observed downregulation of heat shock proteins (e.g. *HSPA1A/B*, *HSP90AA1*, *HSPB1*) and toll-like receptors (e.g. *TLR2*) in prenatal DS microglia (Fig. 3f).

Microenvironmental changes in the prenatal human DS brain
The physical location of cells within a cellular neighborhood can offer insight into both intra- and inter-cellular communication processes that affect tissue and organ development. Therefore, we investigated whether specific cell types exhibit preferential spatial proximity in the human DS brain by employing a general linear mixed effects model on our Slide-seqV2 dataset (Methods). In the ventricular zone, our analysis revealed a sparsity of oRG near IP in DS compared to euploid (Fig. 3g). No significant microarchitectural changes were observed in the cortex (Fig. 3h). Considering that oRG cells differentiate into IPs and play a critical role in supporting an expanded stem cell niche⁴⁹, our findings suggest that oRG cells in DS may undergo functional and positional alterations within the ventricular zone during prenatal development. To enhance the robustness of this tool and minimize the impact of sample variability, we applied a leave-one-subject-out (LOSO)

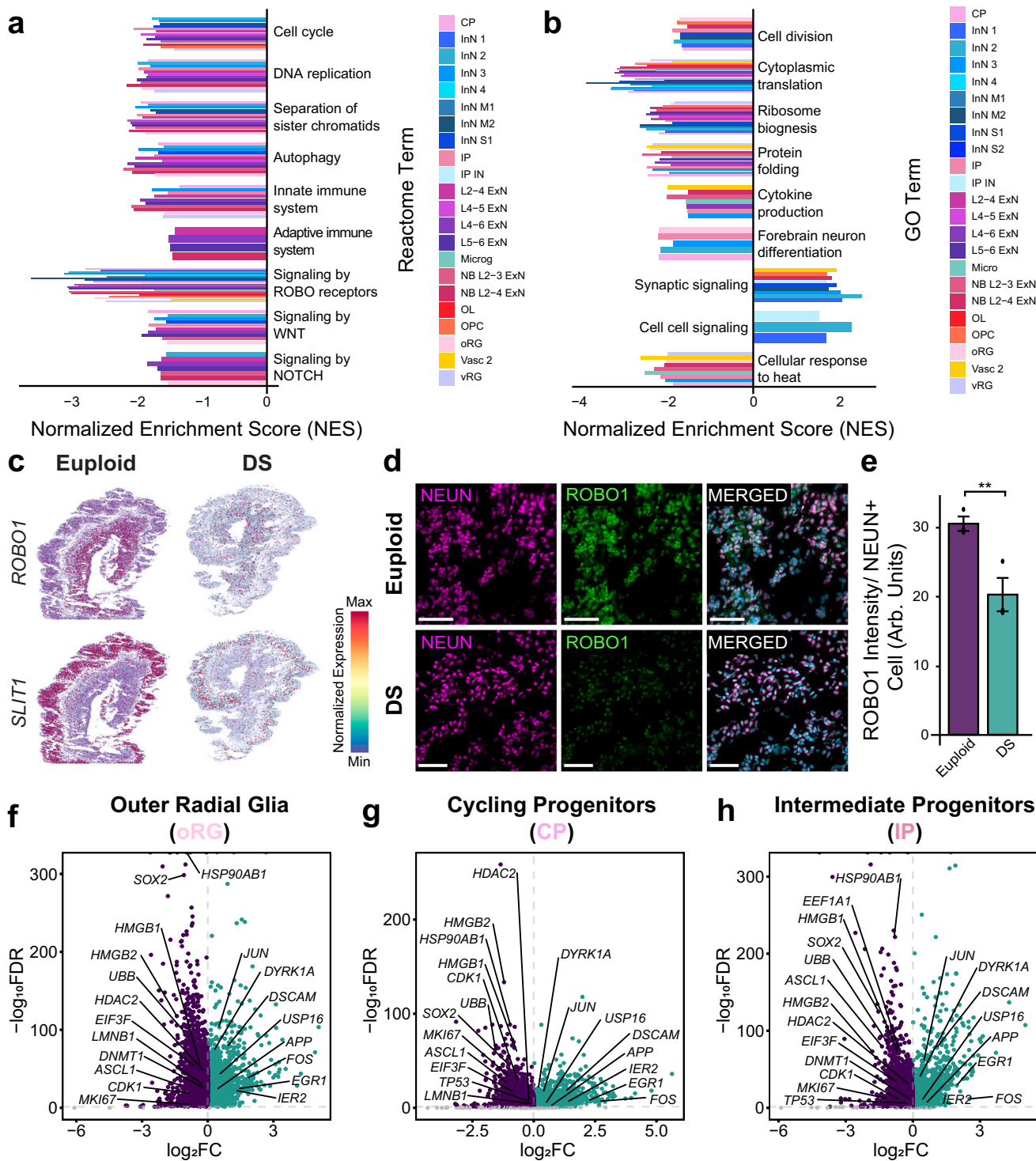


Fig. 2 | Transcriptional dysregulation in neural progenitor cells reveals common themes in the prenatal Down syndrome brain. **a, b**, Barplots of normalized enrichment score (NES) for select **a**, Reactome and **b** gene ontology (GO) biological processes across all cell subtypes identified in the prenatal single-nucleus (sn)RNA-seq dataset. Positive NES values indicate enrichment of gene sets toward the top of the ranked gene list (i.e., genes upregulated in DS), while negative NES values indicate enrichment toward the bottom (i.e., genes downregulated in DS). Comparison is between DS and euploid samples. Bars are colored according to cell subtypes. **c**, Spatial plots of *ROBO1* and *SLT1* in representative Down syndrome (DS) and euploid brains, with gene expression plotted from Slide-seq. Dot color represents normalized gene expression from the 10th to 90th percentiles. **d**, Immunostaining for *ROBO1* (green) in *NEUN*⁺ cells (pink) and DAPI-labeled nuclei (cyan) in a representative prenatal human DS and euploid brain. Scale bar is 50 μm .

e, Bar plots displaying *ROBO1* intensity in *NEUN*⁺ cells, measured in arbitrary units (arb. units). Each dot represents the average intensity for each prenatal human brain ($n = 3$ DS, $n = 3$ euploid). Bars indicate the average intensity per condition, with error bars representing the standard error of the mean. Statistical significance was assessed using a two-sided *t*-test; *p*-value = 0.017. **f–h**, Volcano plots depicting differentially expressed genes (DEGs) in **f**, outer radial glia (oRG), **g**, cycling progenitors (CP), and **h**, intermediate progenitors (IP) from the prenatal human snRNA-seq dataset. Each dot represents a gene and dots are colored according to enrichment: significantly upregulated ($\log_2\text{FC} > 0$, $\text{FDR} \leq 0.05$) in teal, significantly downregulated ($\log_2\text{FC} < 0$, $\text{FDR} \leq 0.05$) in purple, and non-significant genes in gray. Comparison is between DS and euploid samples. The horizontal line depicts $\text{FDR} = 0.05$, and the vertical line depicts $\log_2\text{FC} = 0$.

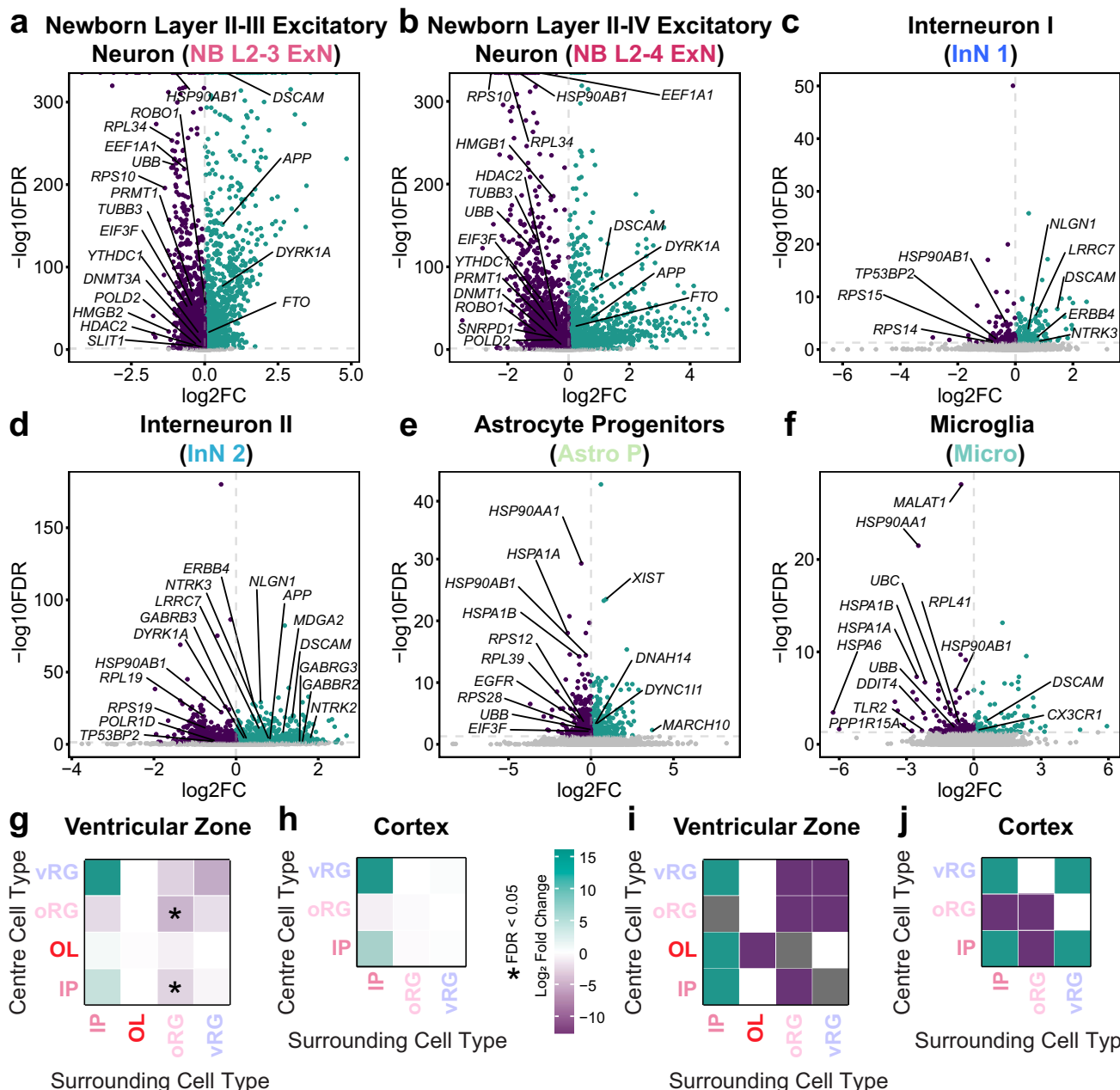


Fig. 3 | Transcriptional signatures of neuronal and glial populations, and cellular compositional changes in the prenatal Down syndrome brain. **a–f** Volcano plots depicting differentially expressed genes (DEGs) in **a** newborn layer II-III excitatory neurons (NB L2-3 ExN), **b** newborn layer II-IV excitatory neurons (NB L2-4 ExN), **c** general interneurons (InN 1), **d** LHX6-expressing interneurons (InN 2), **e** astrocyte progenitors (Astro P), and **f** microglia (Micro) from the prenatal human single-nucleus (sn)RNA-seq dataset. Each dot represents a gene and dots are colored according to enrichment: significantly upregulated ($\log_2\text{FC} > 0$, $\text{FDR} \leq 0.05$) in teal, significantly downregulated ($\log_2\text{FC} < 0$, $\text{FDR} \leq 0.05$) in purple, and non-significant genes in gray. Comparison is between DS and euploid samples. The horizontal line depicts $\text{FDR} = 0.05$, and the vertical line depicts $\log_2\text{FC} = 0$. **g, h** Microenvironment analysis of the Down syndrome (DS) (**g**) ventricular zone (VZ) and (**h**) cortex, from Slide-seq, where a central cell type is selected, and the proportion of the top 100 nearest cells relative to this central cell (y-axis) is calculated in comparison to other cell types of interest (x-axis) and across conditions. Teal indicates an increased abundance of query cells near the central cell in DS compared to control, while purple indicates a decreased abundance. Asterisks (*) denote a false discovery rate (FDR) ≤ 0.05 . **i, j** Leave-one-subject-out (LOSO) analysis across brain region: **i** VZ, **j** cortex. In the LOSO approach, the microenvironmental analysis was iteratively performed while excluding one sample at a time. Mean effect sizes and standard deviations across iterations were used to assess the reproducibility of changes. Teal represents consistently upregulated interactions, purple indicates consistently downregulated interactions, and gray indicates variability in the direction of change across iterations.

and **h** cortex, from Slide-seq, where a central cell type is selected, and the proportion of the top 100 nearest cells relative to this central cell (y-axis) is calculated in comparison to other cell types of interest (x-axis) and across conditions. Teal indicates an increased abundance of query cells near the central cell in DS compared to control, while purple indicates a decreased abundance. Asterisks (*) denote a false discovery rate (FDR) ≤ 0.05 . **i, j** Leave-one-subject-out (LOSO) analysis across brain region: **i** VZ, **j** cortex. In the LOSO approach, the microenvironmental analysis was iteratively performed while excluding one sample at a time. Mean effect sizes and standard deviations across iterations were used to assess the reproducibility of changes. Teal represents consistently upregulated interactions, purple indicates consistently downregulated interactions, and gray indicates variability in the direction of change across iterations.

approach, further reaffirming changes in oRG density near IP in the prenatal DS VZ (Fig. 3*i, j*).

RNA velocity analysis in the prenatal human DS brain

We performed RNA velocity analysis using scVelo⁵⁰ to study the developmental trajectory of cell types in the DS brain, with an emphasis on lineage progression from progenitor fates to mature

neuronal populations. We predicted the future states of cells in our dataset by calculating the ratio of spliced to unspliced mRNA in each cell. While samples in our dataset span gestational ages 13 to 19 PCW, this represents a limited developmental window during gestation, with closely age-matched samples in both conditions. We observed the expected differentiation trajectory from NPCs to IP, and subsequently to newborn and mature ExN and InN, in both euploid and DS

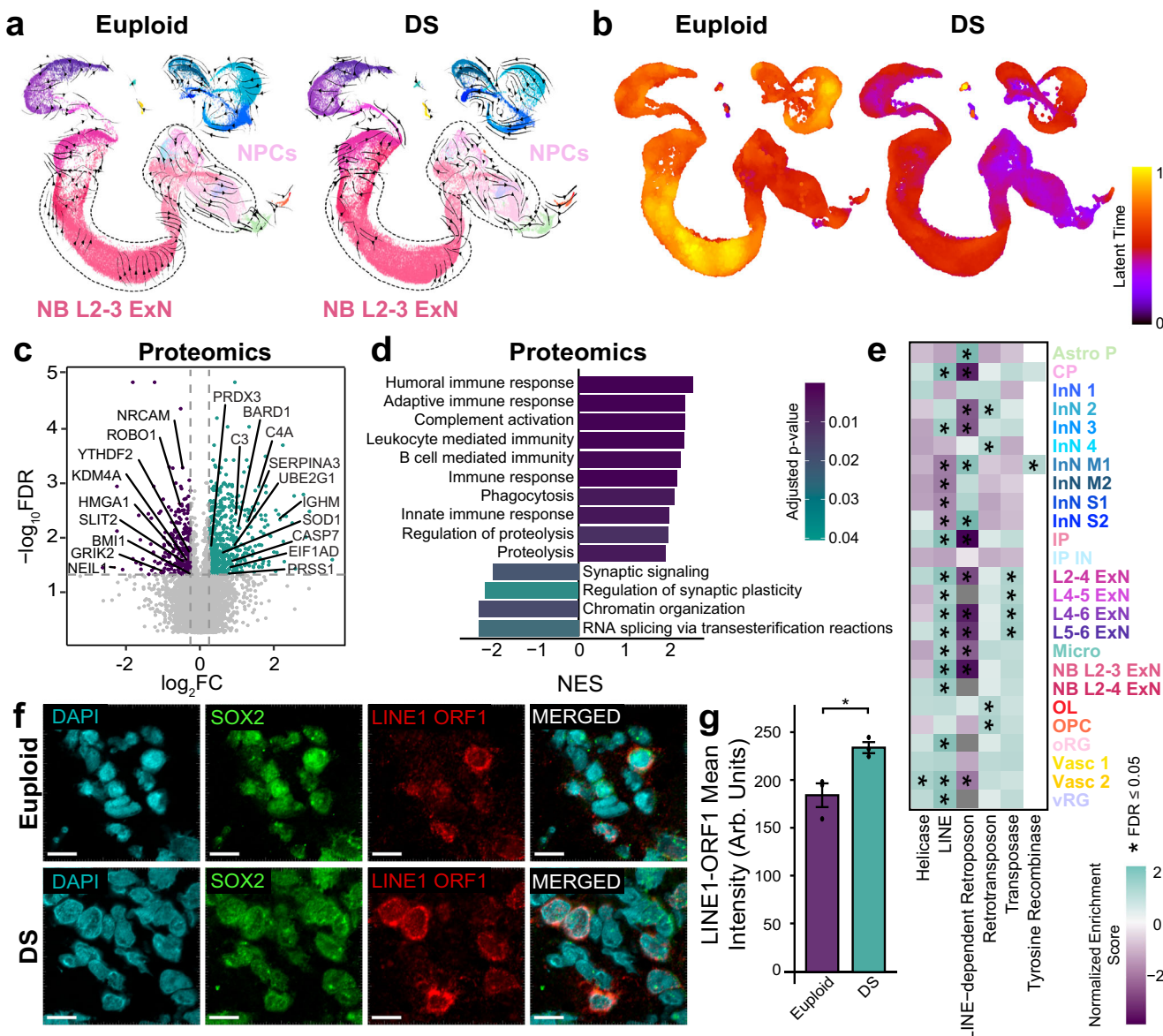


Fig. 4 | The prenatal Down syndrome brain exhibits altered differentiation trajectories and transposable element de-repression. **a** Uniform Manifold Approximation and Projection (UMAP) visualization of RNA velocity trajectory analyses depicting developmental trajectories of cell types within mid-gestational euploid and Down syndrome (DS) brains from the single-nucleus (sn)RNA-seq dataset. Each arrow depicts the estimated direction and magnitude of change between cell states. **b** Latent time projection based on RNA velocity, capturing the relative progression of cells along pseudotemporal differentiation axes within euploid and DS brains. **c** Volcano plots of differential protein abundance from the proteomics analysis ($n = 3$ DS, $n = 4$ euploid). Each dot represents a protein and dots are colored according to enrichment: significantly upregulated ($\log_2 FC \geq 0.25$, $FDR \leq 0.05$) in teal, significantly downregulated ($\log_2 FC \leq -0.25$, $FDR \leq 0.05$) in purple, and non-significant genes in gray. Comparison is between DS and euploid samples. The horizontal line depicts $FDR = 0.05$, and the vertical lines depict $\log_2 FC = 0.25$. **d** Barplot of normalized enrichment score (NES) for select gene ontology (GO) biological processes from the proteomics analysis. Positive NES values indicate pathways enriched among upregulated proteins, while negative NES

values correspond to pathways enriched among downregulated proteins in DS vs euploid. Bars are colored according to the adjusted p-value (FDR), reflecting the statistical significance of the enrichment. **e** Heatmap depicting the NES of transposable element (TE) subclasses in each cell subtype identified in the snRNA-seq dataset. Color reflects NES values, with teal indicating positive enrichment and purple indicating negative enrichment. Comparison is between DS and euploid samples. Gray represents enrichment scores not computed by GSEA. Asterisks (*) denote an $FDR \leq 0.05$. **f** Immunostaining for LINE1-ORF1 (red) in SOX2⁺ (green) and DAPI-labeled nuclei (cyan) cells located near the ventricular zone (VZ) in prenatal human samples. Images are representative of those observed in mid-gestational prenatal euploid and DS brains. Scale bar is 30 μ m. **g** Bar plots displaying LINE1-ORF1 intensity in SOX2⁺ cells, measured in arbitrary units (arb. units). Each dot represents the average intensity for each prenatal human brain ($n = 3$ DS, $n = 3$ euploid). Bars indicate the average intensity per condition, with error bars representing the standard error of the mean. Statistical significance was assessed using a two-sided t-test; p -value = 0.022.

conditions (Fig. 4a). Compared to the euploid brain, the majority of cell types in the DS brain followed a broadly similar differentiation pattern, with a few notable deviations. In particular, we observed differences in RNA dynamics in NPCs, newborn superficial ExN, as well as cortical InN and InN Striatum. In DS NPCs, the reduced directionality

and length of RNA velocity vectors suggest a decelerated differentiation process (Fig. 4a)⁵¹. In newborn superficial NB ExN, the absence of RNA velocity vectors is consistent with a loss of dynamic progression, potentially reflecting reduced cellular activity or terminal differentiation (Fig. 4a). Additionally, more distinct lineage trajectories are

observed in the InN and InN Striatum populations, suggesting a bias in neuronal differentiation toward an inhibitory fate in the DS brain (Fig. 4a). Supporting this observation, latent time analysis—which estimates the relative transcriptional progression of cells along a differentiation trajectory—revealed distinct temporal patterns between conditions. In the euploid brain, latent time increased from NPCs to newborn superficial neurons, reflecting a continuous and ordered maturation process. In contrast, the DS brain displayed uniformly reduced latent times across cell types (Fig. 4b).

We next examined the top-ranked driver genes of cell fate transitions in the human prenatal DS brain. We identified *PAX6*, *TNC*, *EGFR*, and *FOS* as enriched drivers of cell fate in DS ORG and vRG, while these were absent from the top driver genes in euploid counterparts. In addition, examination of the driver genes regulating newborn ExN fate revealed the absence of genes implicated in neuronal state regulation and migration (e.g. *ROBO2*, *SLC11A1*, *DCC*) in the prenatal DS brain. Instead, DS newborn ExN demonstrated driver gene expression of *EOMES* and *PAX6*, which are markers of more immature cell fate (Supplementary Data 4).

Proteomics of the prenatal human DS brain

Previous studies in postmortem DS adult brain tissue have reported altered abundance of proteins involved in RNA splicing and axonal dynamics³⁵, while studies using culture systems have highlighted mitochondrial dysfunction affecting reactive oxygen species homeostasis³². In the present study, we conducted proteomic analysis on seven prenatal human forebrain samples ($n = 4$ DS, $n = 3$ euploid) spanning 13–17 PCW (Supplementary Data 1). 884 proteins had differential abundance between DS and euploid, with 66.7% having increased abundance and 33.3% having decreased abundance ($| \log_2 FC | \geq 0.25$, $FDR \leq 0.05$; Fig. 4c)—all of which are reported in Supplementary Data 5.

In the prenatal DS brain, we observed a robust activation of immune-related pathways, as indicated by enriched GO terms including humoral immune response, complement activation, leukocyte mediated immunity, adaptive immune response, and phagocytosis (Fig. 4d). This immune activation was driven in part by elevated levels of complement proteins (e.g. C1QA/B/C, C1R, C3, C4, C5, C8A/B, C9, CFB) and immunoglobulins (e.g. IGHG1/2, IGHAI, IGHM), which facilitate phagocytosis and opsonization (Fig. 4c). Notably, we also observed enrichment of pathways related to proteolysis and its regulation, reflected by increased levels of proteases (e.g. PRSS1, F2/12), protease inhibitors (e.g. SERPINA3/6/12, SERPINB2, SPINT2, PZP), and ubiquitin-related genes (e.g. UBE2G1, USP16, LTN1) (Fig. 4c).

Beyond the broader pathway-level findings, we identified upregulation of proteins associated with apoptosis (e.g. CASP1/7/14, ELA-POR1, BCL2), oxidative stress response, and reactive oxygen species response (e.g. SOD1, SCARA3, PRDX3, TXNDC5/12, GSTPI) in the prenatal DS brain (Fig. 4c). Several DNA repair proteins also showed altered abundance, with notable upregulation of BARD1, PAXX, EEPD1, MSH3, MMS19, MCM5-7, and WRNIP1, alongside reduced levels of DAXX, SETMAR, NEIL1, and EMSY (Fig. 4c; Supplementary Data 5).

Among the negatively enriched GO terms, we observed downregulation of pathways related to synaptic signaling, regulation of synaptic plasticity, RNA splicing via transesterification reactions, and chromatin organization (Fig. 4d). Specifically, there was a decrease in protein abundance associated with glutamate release (e.g. GRM5/7, GRIK2, SLC1A6), synaptic vesicle trafficking (e.g. AMPH, SCGN, SNAP25, RPH3A), and synaptic adhesion and plasticity (e.g. LRRTM2, CNTNAP4, CBLN1, PCDH17, NRCAM) (Fig. 4c; Supplementary Data 5). Dysregulation of splicing machinery included core spliceosome components (e.g. CWC15, RNF113A) and regulatory factors (e.g. SRSF4, CELF3/5) (Supplementary Data 5). Chromatin-related alterations included reduced abundance of histone demethylases and

transferases (e.g. KDM4A, ASH1L), polycomb group proteins (e.g. BMI1), and high-mobility group proteins (e.g. HMGAI) (Fig. 4c).

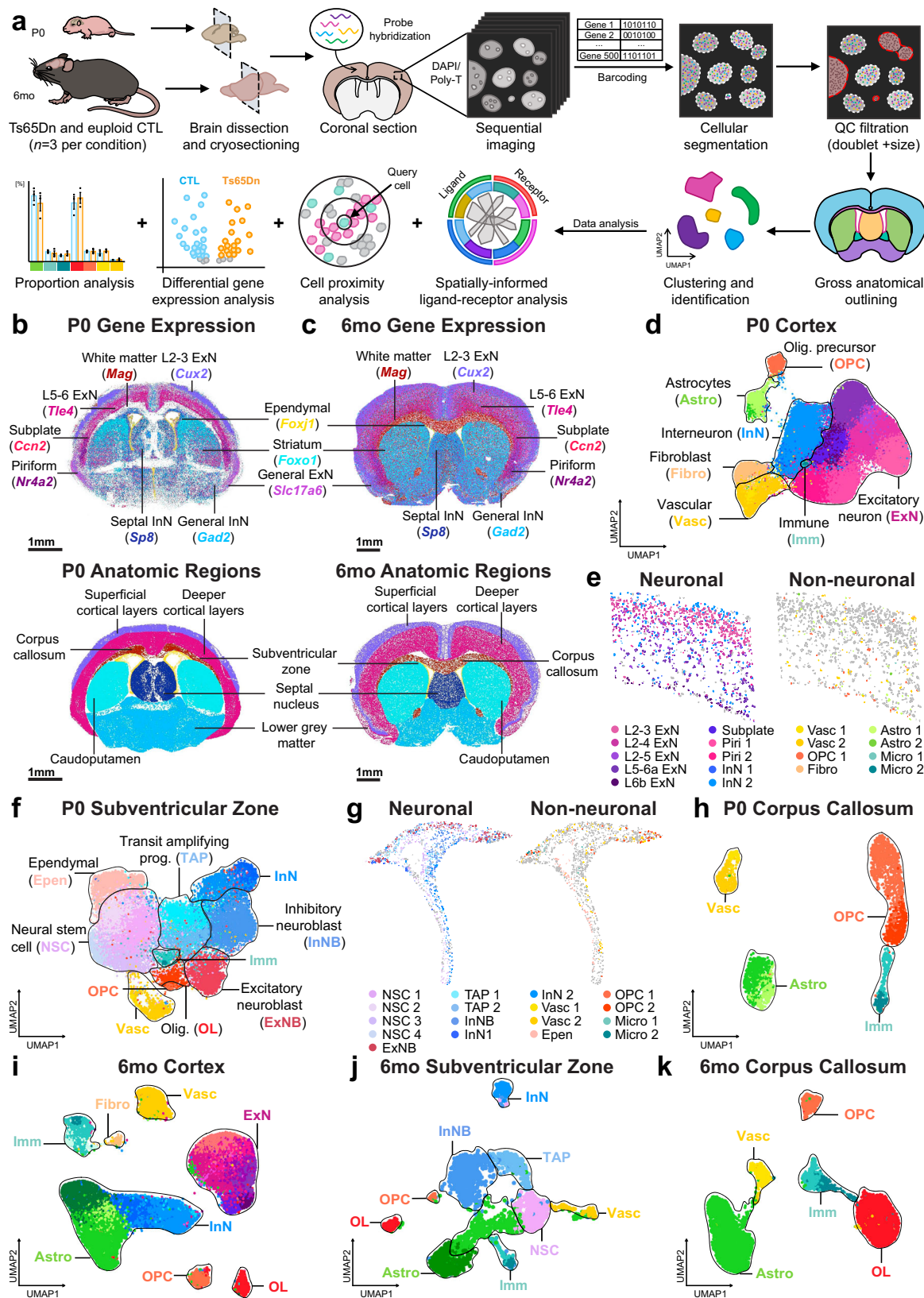
Although our proteomics analysis was not at the single-cell level, we mapped the expression of differentially abundant proteins across cell types using our snRNA-seq dataset (Supplementary Fig. 3a, b). In examining the snRNA-seq and proteomics in tandem, several thematic groups emerged consistently. We identified dysregulation of post-transcriptional processes, including translational regulation (e.g., NOVA1, RBM3, EIF1A, YBX1/3, CNOT2) and m6A RNA modifications (e.g., YTHDF2/3). A second theme was the alteration of chromatin organization, marked by the decrease of chromatin-associated proteins (e.g. DPF3, NUCKS1, WDR70, MACROH2A2) in the prenatal human DS brain (Supplementary Data 2; Supplementary Data 5). Importantly, we also observed reduced abundance of ROBO1 and SLIT2 in the prenatal DS brain (Fig. 4c), consistent with our snRNA-seq findings and immunofluorescence validation.

Transposable element de-repression in the prenatal human DS brain

Both our snRNA-seq and proteomics datasets suggest profound alterations in chromatin remodeling, DNA methylation, and histone modifications in the prenatal DS brain, consistent with recent *in vitro* data showing global chromatin accessibility changes in DS NPCs⁴⁶. Therefore, we hypothesized that alterations in the abundance of chromatin regulators and loss of heterochromatin would lead to aberrant TE mobilization, as has been shown previously^{53,54}. To test this hypothesis, we applied SoloTE³⁵, a tool for analyzing locus-specific TEs, on our snRNA-seq dataset to profile the TE transcriptome during prenatal DS brain development and performed differential analysis between conditions ($| \log_2 FC | > 0$, $FDR \leq 0.05$). All differentially expressed TEs are reported in Supplementary Data 6. Our analysis revealed that the dysregulation of TEs, including DNA transposons and retrotransposons, demonstrated a cell-type-specific pattern (Fig. 4e). Specifically, transposases were exclusively enriched in mature ExN populations of the DS brain, whereas retrotransposons showed enrichment in oligodendrocyte-lineage populations and certain InN populations (Fig. 4e). Perhaps most intriguing was the selective enrichment of long interspersed nuclear elements (LINEs) in DS NPCs, NB and mature ExN, and vascular cells (Fig. 4e; Supplementary Fig. 3c-e). To confirm our finding of aberrant TE mobilization in DS NPCs, we performed immunostaining on prenatal human brain tissue ($n = 3$ DS, $n = 3$ euploid) using a LINE1-ORF1 antibody to detect LINE1 expression (Fig. 4f). NPCs in the DS brain showed a notable increase in LINE1-ORF1 expression in SOX2⁺ cells (p -value = 0.022; Fig. 4g).

In situ spatial transcriptomics of a trisomic mouse model of DS

The Ts65Dn trisomic mouse model is commonly used to study DS⁵⁶. Given the importance of linking human and model system pathobiology, we performed MERFISH on coronal brain sections from P0 ($n = 3$ Ts65Dn, $n = 3$ euploid) and 6mo ($n = 3$ Ts65Dn, $n = 3$ euploid) male Ts65Dn mice and littermate euploids (Fig. 5a), as these timepoints reflect both early and mature developmental processes across a broad age range. A panel of 500 genes was curated to identify major brain cell types, as well as biologically relevant signaling pathways, inflammatory and immune-related markers, senescence-associated signatures, and extracellular matrix components pertaining to neurogenesis (Supplementary Data 7). Cells were subjected to stringent QC filtering—including volume, transcript, and doublet removal—normalization, and batch correction (Methods). The number of genes, transcripts, and mitochondrial RNA were consistent across all samples, yielding a median of 321.9 transcripts per cell in the P0 dataset, and 497.4 transcripts per cell in the 6mo dataset (Supplementary Fig. 4a-f). The spatial distribution of canonical cell type markers and the Allen Brain Atlas⁵⁷ were used to label gross anatomical regions within the P0 and 6mo datasets, including the



superficial and deeper cortical layers, subventricular zone, corpus callosum, caudoputamen, septal nucleus, and lower gray matter (Methods; Fig. 5b, c). Dimensionality reduction using principal component analysis (PCA), unsupervised clustering using uniform manifold approximation and projection (sNN) clustering were performed on each region in the P0 and 6mo datasets.

In the P0 cortex, we identified 12 major clusters corresponding to the following cell populations: ExN expressing *Cux2*, *Mef2c*, *Slc17a6*; InN expressing *Gad1* or *Gad2*; astrocytes expressing *Aqp4*, *Gfap*, and *Slc1a3*; OPCs expressing *Pdgfra*, *Sox10*, and *Olig1*; vascular cells expressing *Pdgfrb*, *Kcnj8*, and *Pecam1*; microglia expressing *Cx3cr1* and *Tmem119*; and fibroblasts (Fibro) expressed *Fbln1* (Fig. 5d;

Fig. 5 | Cellular and spatial landscape of postnatal and mature trisomic mouse brains. **a** Schematic overview of the MERFISH pipeline. **b, c** Spatial distribution of select cell type markers and segmentation of major anatomical regions on a representative **b**, postnatal (PO) and **c** 6 month (6mo) brain sample. **d** Uniform Manifold Approximation and Projection (UMAP) representation of the PO cortex. Each dot represents a cell. Cell types are delineated by the solid line and cell subtypes are denoted by different shades. **e** Spatial distribution of cell subtypes

on a cross-section of the PO cortex. Each dot represents an individual cell and is color-coded based on cell subtype identity. **f** UMAP representation of the PO subventricular zone. **g** Spatial distribution of cell subtypes within the subventricular zone of the left hemisphere in the PO brain. Each dot represents an individual cell and is color-coded based on cell subtype identity. **h** UMAP representation of the PO subventricular zone. UMAP representations of the 6mo **i** cortex, **j** subventricular zone, and **k** corpus callosum.

Supplementary Fig. 5a). Spatial mapping of neuronal and non-neuronal cells accurately reflected their respective cell type annotations within the PO cortex (Fig. 5e). In the PO subventricular zone, 11 major clusters corresponding to neural stem cells (NSCs) expressing *Clu*, *Aldoc*, *Fabp7*; transit amplifying progenitors (TAPs) expressing *Mki67*, *Ascl1*, and *Arx*; excitatory neuroblast (ExNB) expressing *Slc17a6* and *Dcx*; inhibitory neuroblast expressing *Gad1* and *Dcx*; ependymal cells expressing *Foxj1* (Fig. 5f; Supplementary Fig. 5b). The spatial mapping of NPCs and non-neuronal cells in the PO subventricular zone confirmed their corresponding cell type annotations (Fig. 5g). In the PO corpus callosum, eight major clusters corresponding to OPCs, Astro, vascular, and microglia were identified (Fig. 5h; Supplementary Fig. 5c).

Next, we selected broad cell types and conducted iterative clustering analyses to characterize cell subtypes in the PO dataset, as well as in the 6mo cortex (Fig. 5i; Supplementary Fig. 5d), subventricular zone (Fig. 5j; Supplementary Fig. 5e), and corpus callosum (Fig. 5k, Supplementary Fig. 5f; Methods). We identified a diverse taxonomy of cell subtypes that were organized by spatial location. No significant changes in the proportion of neuronal, glial, and non-neuronal cells were observed in the PO and 6mo cortex, corpus callosum, or subventricular zone (Supplementary Fig. 6a–f).

Differential gene expression analysis in the Ts65Dn brain

To identify changes in molecular processes perturbed during early life neurodevelopment and maturation, we compared spatial gene expression between Ts65Dn and euploid mice within the same cell types and region. DEGs were identified in nearly every cell type in the PO and 6mo cortex, subventricular zone, and corpus callosum (Supplementary Data 8). In trisomic PO NPCs, including NSCs (Fig. 6a), TAPs (Fig. 6b), and ExNB (Fig. 6c), we identified significant dysregulation in several signaling pathways. Specifically, the WNT pathway showed upregulation of *Dvl1*, *Fzd7/8*, *Lrp5/6*, *Gsk3b*, and *Dkk3*, alongside downregulation of *Apc*, *Fzd5*, *Rac1*, and *Csnk1a1*. The SHH pathway exhibited upregulation of *Sufu*, and *Gli2/3*, with downregulation of *Nras* and *Fgfr2*. Additionally, the NOTCH pathway demonstrated upregulation of *Notch 1/2/3*, *Rcan1*, *Hes1*, and *Tle1/3*, and downregulation of *Tle4* and *Itch* in Ts65Dn mice (Fig. 6a–c; Supplementary Data 8).

These changes in trisomic NPCs were accompanied by disruptions in genes associated with transcriptional and translational regulation, including *Ep300* and *Eif4g1*, as well as tRNA synthetases such as *Wars*, *Qars* and *Vars2*, and epitranscriptomic factors including *Fto*, *Ythdc1*, *Ythdf1*, *Alkbh5*, and *Igfbp2* (Fig. 6a–c). The expression of genes integral to various DNA repair pathways was altered in trisomic mice, including those involved in double-strand break repair such as *Rad50*, *Topbp1*, *Nbn*, and *Atm*; cell cycle checkpoint regulators, such as *Hus1*, *Cdkn1c*, *Ccna2*, *Ccne2*, and *Trp53*; and DNA damage response, such as *Chek2* (Supplementary Data 8).

Key genes involved in regulating NSC self-renewal, proliferation, and maintenance, such as *Vcam1*, *Rac1*, *Creb1*, *Jak1/2*, *Sirt1*, *Mapk1*, and *Fgfr2*, as well as the astrocytic markers *Fabp7* and *Slc1a3*, were downregulated in trisomic NSCs (Fig. 6a; Supplementary Data 8). Previous reports have shown that NSC proliferation in neurogenic niches was reduced in a cell-autonomous manner following the knockdown of *Fabp7* and *Slc1a3*^{58,59}. The transcription factor *Olig2*, a known triplicated gene in Ts65Dn and key regulator of oligodendrocyte differentiation⁶⁰, was upregulated in trisomic NSCs. Overexpression of

Olig2 is known to also impair NSC proliferation, induce premature cell cycle exit of InN precursors, and downregulate pro-neural factors⁶¹. As cells progressed towards TAPs and NBs, we observed downregulation of proliferation markers *Mki67* and *Egr1*, the nuclear lamina marker *Lmnbl1*, along with migration markers *Unc5d*, *Dcx*, *Satb2*, and *Rac1* (Fig. 6b, c). In 6mo mice, trisomic NPCs showed elevated levels of mature astrocytic markers, including *Gfap* and *Aqp4* (Supplementary Data 8).

Microarchitectural changes in Ts65Dn brain development

We next investigated whether trisomy is associated with changes to the composition of the cellular microenvironment in our mouse model, as we did in the human brain (Methods). In the trisomic PO corpus callosum, we found an enrichment of microglia cells near OPCs, while also observing a sparsity of OPCs near astrocytes (Fig. 6d). In the trisomic PO and 6mo cortex, we found fewer OPCs near deep-layer ExN (Supplementary Fig. 7a, b). No significant changes were identified in the PO subventricular zone (Supplementary Fig. 7c). Fewer astrocytes were observed near OPCs, OLs, vascular cells, ExN, and InN in the trisomic 6mo cortex (Supplementary Fig. 7b). No significant micro-environmental changes were identified in the 6mo corpus callosum (Supplementary Fig. 7d). The presence of astrocytes near TAPs was increased in the trisomic 6mo subventricular zone (Fig. 6e) suggesting the involvement of glial cells in regulating adult neurogenesis and shaping neuronal precursor development. Application of the LOSO approach across datasets yielded consistent results, supporting the robustness of our findings and indicating that observed changes are not driven by individual biological variability (Supplementary Fig. 7e–j).

Comparisons between human and Ts65Dn datasets

We identified both overlapping and divergent patterns of molecular dysregulation between the human and mouse datasets, which is unsurprising given previous literature noting limitations of the Ts65Dn mouse model⁶². In the prenatal human brain, we identified widespread post-transcriptional dysregulation across multiple levels within the NPC population, spanning translation initiation and elongation (e.g., *EIF3F*), the epitranscriptome (e.g., *YTHDF2/3*), ribosomal function, and peptide processing (e.g., *RPL18*). In PO Ts65Dn NPCs, despite our analysis being limited to a focused gene panel, we similarly observed dysregulation of genes at several of these regulatory layers, including translational machinery (e.g., *Eif4g1*), the epitranscriptome (e.g., *Ythdc1*), and tRNA synthetases (e.g., *Qars*). Another recurring theme of dysregulation in both datasets included genes associated with DNA repair and cell cycle regulation, including checkpoint control (e.g., *TP53*; *Trp53*) and cyclin-related genes (e.g., *CDKN1B*; *Cdkn1c*), particularly in NPCs.

Proteomic analysis from the prenatal human brain showed broad upregulation of immune-related proteins, including components of both innate and adaptive immune pathways. In contrast, immune gene dysregulation was comparatively limited across development in the Ts65Dn data. Key interferon signaling components, such as *Ifnar1/2* and *Irf3*, showed minimal differential expression in cortical microglia and astrocyte populations (Supplementary Data 8). However, by six months of age, expression of the interferon GTPase *Mx1* emerged across multiple cortical cell types, potentially signaling the early stages of a neuroinflammatory response (Supplementary Data 8).

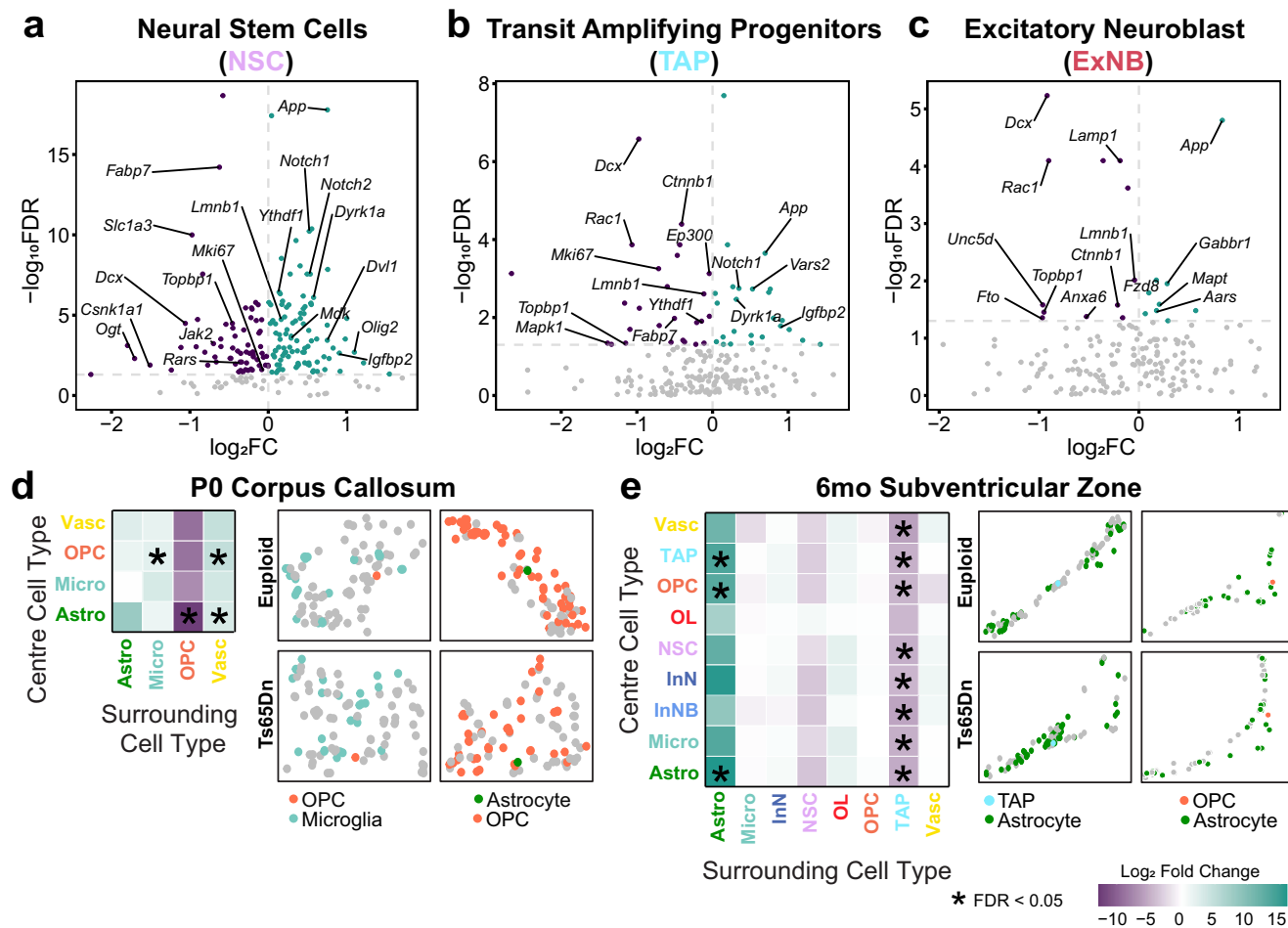


Fig. 6 | Down syndrome-associated transcriptional and local cellular architecture changes in trisomic mice. **a–c** Volcano plots depicting differentially expressed genes (DEGs) in **(a)**, neural stem cells (NSCs), **(b)** transit amplifying progenitors (TAPs), and **(c)** excitatory neuroblasts (ExNB) from the postnatal (P0) MERFISH subventricular zone (SVZ) dataset. Each dot represents a gene and dots are colored according to enrichment: significantly upregulated ($\log_2\text{FC} > 0$, $\text{FDR} \leq 0.05$) in teal, significantly downregulated ($\log_2\text{FC} < 0$, $\text{FDR} \leq 0.05$) in purple, and non-significant genes in gray. Comparison is between Ts65Dn and euploid samples. The horizontal line depicts $\text{FDR} = 0.05$, and the vertical line depicts $\log_2\text{FC} = 0$. **d** Microenvironment analysis of the P0 corpus callosum and spatial plots depicting increased proximity of microglia surrounding oligodendrocyte progenitor cells

(OPCs) and decreased proximity of OPCs surrounding astrocytes in Ts65Dn relative to euploid. In this analysis, a central cell type is selected, and the proportion of the top 100 nearest cells relative to this central cell (y-axis) is calculated in comparison to other cell types of interest (x-axis) and across conditions, with corrections made using the Benjamini-Hochberg method. Teal indicates an increased abundance of query cells near the central cell in Ts65Dn compared to control, while purple indicates a decreased abundance of query cells near the central cell in Ts65Dn compared to control. Asterisks denote $\text{FDR} \leq 0.05$. **e** Microenvironment analysis of the 6mo subventricular zone and spatial plots depicting increased proximity of astrocytes surrounding transit amplifying cells (TAPs) and OPCs in Ts65Dn relative to euploid.

One key finding from our human DS dataset was widespread TE activation across multiple cell types, with elevated expression of LINE1 elements in NPCs and ExN. To investigate the presence of aberrant TE expression in the 6mo Ts65Dn model ($n = 3$ Ts65Dn, $n = 3$ euploid), we applied the SoloTE pipeline to a previously published snRNA-seq dataset⁶³ and performed differential analysis between conditions—the results of which are reported in Supplementary Data 9. Globally, TEs did not demonstrate the same degree of cell type-specific de-repression as in the human dataset (Supplementary Fig. 7k). We observed cell type-specific enrichment of distinct TE subfamilies, including retrotransposons in InN and OPCs, transposases in microglia, and helicases in fibroblasts, in Ts65Dn compared to euploid controls (Supplementary Fig. 7l). The mechanisms of cell type- and developmentally regulated TE activation in the DS brain thus warrant further experimental investigation.

Discussion

DS poses a unique and complex neurobiological challenge given the multicellular impact of Hsa21 triplication and the subsequent cascade

of developmental consequences. The early life origins of cortical disorganization are poorly understood in DS, as are the mechanisms of disrupted neurogenesis and gliogenesis. In this study, we created an atlas of the molecular and cellular architecture of the human DS and trisomic mouse brain. We profiled $> 120,000$ cells in the prenatal human brain by snRNA-seq and $> 240,000$ cells in the mouse brain by MERFISH to characterize developmental and brain region-specific gene programs that are disrupted. Given the need to bridge the translational gap between mouse models and human disease, this study serves as an important discovery platform for uncovering conserved and divergent DS-associated pathomechanisms.

Herein, we provide a taxonomy of cellular diversity in the DS brain, characterizing DEGs and alterations to cellular architecture in the human and mouse. In the prenatal human brain, we identify profound transcriptional changes in NPCs, including signatures of altered post-transcriptional regulation, as well as altered cell fate and migration. Our findings from the prenatal human brain support recently published studies that show significant changes to 3D genome structure, chromatin accessibility, and human DS NPC senescence

in vitro^{35,46,64}. While we observed downregulation of nuclear markers associated with senescence (e.g., *LMNB1*, *TP53*, *HMGBl/2*), we did not detect upregulation of senescence-associated secretory phenotype (SASP) markers or cyclin-dependent kinase inhibitors, suggesting the absence of a full senescent phenotype at this developmental stage. The broad transcriptional downregulation of key chromatin regulators (e.g., *HDAC1/2*, *EZH2*, *EED*, *KAT2A*, *AURKB*, *VRKI*) may suggest a chromatin landscape that is permissive to senescence-like states^{46,65,66}. This partial phenotype may reflect a state of replicative stress in NPCs, consistent with the progeroid features of DS and the known association of senescence with developmental timing and genomic instability in related syndromes⁶⁷. Importantly, this interpretation highlights the need for longitudinal studies across multiple timepoints to define the temporal onset of senescence and its contribution to DS neuropathology. In addition, we identify profound downregulation of SLIT-ROBO signaling in the prenatal human DS brain, implying that disruptions to canonical guidance cues necessary for neuronal precursor and cortical neuron migration may contribute to cortical dysplasia⁶⁸. We also reveal the altered spatial positioning of DS oRG in the ventricular zone.

Further, both our transcriptomics and proteomics data suggest common mis-regulation of genome integrity, cell cycle regulation, and DNA damage response during prenatal DS brain development. This builds upon previous studies that have characterized disruption in mRNA translational machinery and genotoxic stress, as well as global immune remodeling in the DS brain^{69–71}. Interestingly, our proteomics analysis reveals hyperactivation of the complement system during gestational DS development, potentially triggering proteolytic cascades and the classical inflammatory response, while also enhancing both innate and adaptive immune activity⁷². Hyperactivation of the immune system may play a significant role in neuroinflammation during gestation, which is known to contribute to long-term alterations in brain development⁷³. Additionally, the complement system is involved in the radial migration of pyramidal ExN and InN during normal brain development^{74,75}. While further research is needed to validate the role of complement activation during prenatal DS brain development, our proteomics findings implicate this pathway in abnormal DS corticogenesis.

A notable finding from our study is the lineage-restricted activation of TEs in the human prenatal DS brain, including aberrant de-repression of LINEs in DS NPCs and ExN. LINEs have been reported to be non-randomly activated during neurogenesis, safeguarding NPCs from precocious differentiation⁷⁶ while also functioning as potent cis-regulatory elements that influence gene expression⁷⁷. In humans and mice, LINEs have also been reported to act as long non-coding RNAs, playing key roles in regulating NPC differentiation, migration of post-mitotic neurons, and affecting cell type proportions^{78,79}. Based on these established functions, we propose that de-repression of TEs as an emerging hallmark of DS that may contribute to altered neural fate specification, impaired corticogenesis, innate and adaptive immune activation, and potentially accelerated aging. Interestingly, we did not identify evidence of the cytosolic DNA-sensing cGAS/STING activation in snRNA-seq or proteomics. However, by proteomics we observed the downregulation of VPS37A (Supplementary Data 5), a core component of the endosomal sorting complex required for transport (ESCRT-I) that has been implicated in regulation of LINE retrotransposition⁸⁰. Further work is needed to understand mechanisms of LINE1 activity in the prenatal human DS brain. Additionally, while this present study did not directly investigate the specific mechanisms by which Hsa21 triplication influences TE de-repression, it is plausible that over-expression of certain epigenetic regulators encoded on Hsa21 contributes to this phenomenon early in development. Genes such as *DNMT3L*, *N6AMT1*, *MIS18A*, *DYRK1A*, *HMGNI*, which are involved in DNA methylation and chromatin maintenance, may disrupt the epigenetic landscape through gene-specific or multi-gene cascades, thereby

facilitating LINE1 and other TE activation^{77,81,82}. Future work focused on dissecting the role of these genes, individually and in combination, will be essential in elucidating their impact on TE regulation and downstream effects on NPC development in DS.

In the P0 Ts65Dn mice, NPCs show mis-expression of genes associated with key neurodevelopmental processes, including self-renewal, differentiation, and migration, consistent with prior studies reporting reduced proliferative capacity in neonatal Ts65Dn NSCs⁸³. Notably, the downregulation of *Mki67* and *Dcx* suggests impairments in proliferative capacity and neuroblast migration, consistent with prior observations of reduced cycling cells in S phase in the neurogenic regions such as the dentate gyrus and lateral ventricle⁸⁴. Our transcriptional analysis supports the concept of early-stage progenitor dysfunction resulting from longer cycle duration and reduced neurogenesis⁸³. Such deficits likely underlie hypocellularity and disrupted cortical development observed postnatally, suggesting that cell cycle alterations in Ts65Dn NPCs may be a key mechanistic driver of downstream neurodevelopmental abnormalities. However, the precise molecular drivers and temporal onset of these impairments warrant further mechanistic investigations.

By 6 months of age, the NSC transcriptional profile shifts, reflecting changes associated with glial lineage specification. This temporal transition coincides with morphological and molecular alterations in the neurogenic niche, most notably an increased astrocytic presence around TAPs. The elevated expression of astrocytic markers such as *Gfap* and *Aqp4* at this stage is suggestive of an emerging reactive glial phenotype, consistent with prior reports of astrocyte hypertrophy and proliferation that arise during DS aging^{85,86}—supporting the model of progressive astrogliosis and neuroinflammation in DS.

Our study has several technical and conceptual limitations. There are potential inconsistencies in the anatomical plane of sectioning and quality of prenatal human brain tissue, given the nature of postmortem tissue. However, only similar brain regions were compared for differential analysis. Prenatal human brain tissue was studied over a narrow mid-gestational window due to the pragmatic limitations on obtaining this tissue. Sample size may be a further limitation, and future studies with expanded cohorts of human prenatal tissue could provide additional insights. Imaging and slide-based spatial transcriptomics methods each have advantages and limitations, including differences in resolution, which have been reviewed elsewhere⁸⁷. MERFISH, like other imaging-based spatial transcriptomics, relies on cell boundary segmentation to assign transcripts to cells, which can lead to false transcript assignment⁸⁸. This was mitigated through the use of rigorous quality control filtering across datasets. MERFISH also relies on a manually curated list of finite gene targets, which biases the potential findings and conclusions. The Ts65Dn trisomic mouse model is widely used but has significant biological limitations in the extrapolation to the human condition^{89,90}.

This work is primarily intended as a resource and discovery dataset to generate hypotheses for future mechanistic study. This work underscores the importance of investigating mechanisms of NPC dysfunction in DS, as this may be an early driver of abnormal corticogenesis. Specifically, experiments should explore the biological cascade triggering TE de-repression. Does NPC senescence and ensuing loss in chromatin structure, as described by Meharena et al.⁴⁶, trigger TE-depression, or is the converse true, with TE de-repression triggered through loss of heterochromatin, which may then promote senescence? Recent studies have shown promising results using reverse transcriptase inhibitors to target TEs in trisomic mice⁹¹, but implications in human NPCs are unclear. Our work also highlights changes in gene programs associated with cell migration (e.g. ROBO/SLIT), and this may benefit from experiments in human organoids. Additionally, future studies in alternative DS mouse models, such as the Ts66Yah, which lacks triplication of genomic regions unrelated to

Hsa21⁹², will be important to define model-specific changes and human disease relevance.

Despite limitations, our extensive cross-species resource of spatially informed gene expression in the DS brain provides important insights into candidate signaling pathways and molecular processes that are targetable in DS.

Methods

Human sample collection for snRNA-seq and Slide-seq

Prenatal human brain samples (13–19 gestational weeks) were obtained from the Human Developmental Biology Resource (HDBR, United Kingdom), under a research ethics agreement from Clinical Trials Ontario (Study # 3227). Postmortem interval (PMI) for HDBR samples ranged between 30 min to 3 hours and were transported to the clinic in PBS media. Ten fresh-frozen brain tissues ($n = 5$ DS, $n = 5$ euploid) were obtained for snRNA-seq and stored at -80°C until processing. Six optimal cutting temperature compound-embedded (OCT) brain tissue ($n = 3$ DS, $n = 3$ euploid) were obtained for Slide-Seq and stored at -80°C until processing. Eight fresh-frozen brain tissues ($n = 4$ DS, $n = 4$ euploid) were obtained for proteomics and stored at -80°C until processing. (Supplementary Data 1). Trisomy 21 was confirmed by karyotyping. Samples were kept on dry ice as long as possible to preserve RNA integrity during downstream processing.

Human tissue sample dissection, nuclei isolation, and RNA preparation for snRNA-seq

Nuclei were extracted from ten individual brain samples and processed using the 10x Genomics Chromium System. Libraries were sequenced using the Novaseq 6000 on S1 flow cell at the Centre for Applied Genomics (TCAG; The Hospital for Sick Children) in Toronto, ON, Canada. To ensure data quality, cells from individual replicates underwent stringent quality control filtering and were normalized using SCTtransform. Cells with $\geq 5\%$ mitochondrial genes, ≤ 200 , and $\geq 2,500$ unique feature counts were excluded from the datasets. Following, individual replicates were integrated, and Harmony was used to correct for potential batch effects. Seurat v5 (RRID:SCR_016341) was used to perform data normalization, dimensional reduction using PCA, and graph-based clustering with UMAP.

snRNA-seq granular cell type identification and automated cell type transfer

Cluster identity was assigned by using known literature cell type annotations and described in the main text. Sub-clustering within each broad cell type with batch effect correction was performed to identify granular cell subtypes. Within vascular cells, we found a pericyte population (Vasc 1) expressing *PDGFRB* and *RGSS5*, and an endothelial population (Vasc 2) expressing *PECAM1*, *ESAM*, and *CLDN5*. Re-clustering of immune cells revealed one population of homeostatic microglia (Micro 1) expressing *ITGAM*, *CSF1R*, and *PTPRC*, while lacking phagocytic (*AIF1*, *CD68*) and reactive markers (*TREM2*). We identified one population of astrocyte progenitors expressing *SLC1A3*, *NFIA*, and *TNC*, while lacking mature markers (*AQP4*). To confirm our cell type labeling, we performed automated cell type transfer using a developing human brain dataset⁹³ and whole mouse brain dataset⁹⁴ using CellTypist⁹⁵.

Human tissue sectioning and Slide-seq preparation

Cryosectioning was performed with consideration of anatomical landmarks, specifically targeting regions where the ventricular zone or cortical layers were discernible. OCT-embedded brain tissue was sectioned at a thickness of 10 μm at -21°C using the CM1950 Leica cryostat and immediately mounted onto a 10 \times 10 mm Slide-seq chip. In cases where the tissue covered less than 50% of the tile, an additional serial section was placed adjacently on the same tile to increase coverage. Libraries were sequenced on a Novaseq X flowcell 10B (100

cycles). Genome alignment, filtration, and normalization were performed using the Curio Seeker bioinformatic pipeline as per the manufacturer's recommendations.

Slide-Seq bioinformatic analysis

To reconstruct the spatial mapping of gene expression, the Curio Seeker bioinformatics pipeline was performed according to the manufacturer's protocol using the GRCh37 genome reference from UCSC. Pixels with $\geq 5\%$ mitochondrial genes and ≤ 200 unique features were excluded from the dataset. RCTD was used to decompose RNA sequencing mixtures into individual cell, referencing our human snRNA-seq dataset after excluding InN striatal cell types, given the striatum was not represented in the spatial dataset⁹⁶. Doublets uncertain and rejects were removed from the final object prior to downstream analyses. As the entirety of the tile was not covered by tissue, we adapted the CellSelector tool in Seurat v5 (RRID:SCR_016341) to select one sample per tile, remove additional off-target beads and demarcate the ventricular zone and cortex for each individual sample⁹⁷. Replicates were then normalized using SCTtransform, integrated, and scaled using Seurat v5 (R v4.2.1).

Proportion analysis

To identify changes in the relative abundance of cell types during DS neurodevelopment in our human and mouse datasets, we computed the proportion of cells for a specific subtype by dividing its count by the total number of cells in the respective replicate. Statistical significance was calculated using an unpaired two-tailed *t*-test, and corrections for multiple comparisons were implemented using Benjamini-Hochberg (BH).

Differential gene expression analysis and pathway analysis

DGE analysis was performed using the MAST framework, applying two-sided tests and using biological replicate identity as a covariate to minimize inter-sample variability and improve detection of condition-specific transcriptional changes. FDR correction was applied using the BH method across all datasets. Genes expressed in at least 5% of nuclei within each cell subtype were retained. For the human snRNA-seq dataset, raw UMI counts were extracted from the "RNA assay" of the Seurat object and normalized. For the human snRNA-seq dataset, genes with $|\log_2\text{FC}| > 0$ and $\text{FDR} \leq 0.05$ were considered statistically significant. A $|\log_2\text{FC}| > 0$ and $\text{FDR} \leq 0.05$ were used for the MERFISH datasets. Functional enrichment analysis was performed for DEGs within each cell subtype using GSEA. Pathway analysis was conducted using GO Biological Processes and Reactome databases with the ClusterProfiler package (v4.10.1). Statistically significant enrichment for GO pathways were determined with $\text{FDR} \leq 0.05$. Manual selection of relevant pathways was plotted in the figures.

RNA velocity

BAM files from individual snRNA-seq replicates were preprocessed using the Velocyto command line in Velocyto v0.17.17⁹⁸. The human reference genome GRCh38/hg38 was retrieved from the UCSC genome browser. Output loom files from individual replicates were integrated to generate a new count matrix with the top 2000 variable features. Two additional count matrices were generated to separate the DS and euploid conditions. Following, scVelo v0.3.1⁹⁹ was used to compute expression dynamics and latent time for all three count matrices in Python.

Transposable element analysis

BAM files from individual snRNA-seq replicates, containing GN and CB tags, were used as input files for the SoloTE (v1.09) tool⁵⁵. To optimize our alignment for the detection of multi-mapped reads, the STAR parameters were set to --winAnchorMultimapNmax 100 and --outFilterMultimapNmax 100. SoloTE selected reads that were not mapped

to known genes to avoid false identification of gene-associated TEs as independent transcriptional units. Dual analysis, where reads mapped to genes, were also included in our analysis. BEDtools was used to assess the overlap between filtered reads and transposable element annotations. Expression levels were quantified at the locus level for reads with high mapping quality, while multi-mapped reads were aggregated at the subfamily level. The Dfam⁹⁹ and Repbase¹⁰⁰ databases were used to categorize the TEs into subfamilies of DNA transposons and retrotransposons. Following, DEG analysis using the MAST framework with two-sided testing and FDR correction using BH ($|\log_2\text{FC}| > 0$; $\text{FDR} \leq 0.05$) was performed between conditions to identify DS-specific enrichment of TEs. Granular cell subtype-specific enrichment of TEs was performed using GSEA.

Immunofluorescence and Antigen Retrieval

Human prenatal brain tissue sections were incubated at 37°C for 30 min, washed 1x in 1x PBS for 15 min, fixed with 70% methanol on ice for 10 min, washed 1x in 1x PBS for 5 min, incubated with 70% methanol on ice for 5 min, or fixed with 4% paraformaldehyde for 7 min, washed 3x in 1x PBS for 15 min each, and incubated with normal donkey serum blocking buffer (AB_2337254) at room temperature for 1 hour. Antigen retrieval was performed for the LINE1-ORF1p antibody using Tris/EDTA pH 9.0 buffer solution in a microwave, following the Abcam protocol (<https://www.abcam.com/en-us/technical-resources/protocols/ihc-antigen-retrieval>). The primary antibodies used for IF were goat anti-SOX2 (1:200, Abcam, catalog #Af2018), rabbit anti-LMNB1 (1:150, Abcam, #Ab16048), rabbit anti-LINE1 ORF1p antibody (1:50, Abcam, #Ab216324), mouse p53 antibody (1:200, Santa Cruz, #sc-126), mouse anti-NeuN antibody (1:200, Millipore, #MAB377), and goat ROBO1 antibody (1:100, Thermo Fisher, #PA5-18460). The secondary antibodies used for IF were Alexa Fluor 488 donkey anti-goat IgG (1:500, ThermoFisher, catalog #A-31573), Alexa Fluor 555 donkey anti-mouse IgG (1:500, ThermoFisher, catalog #A-31570), Alexa Fluor 647 donkey anti-rabbit (1:500, ThermoFisher, catalog #A-31573).

Confocal imaging and fluorescence intensity quantification

High magnification confocal images of LMNB1/SOX2, LINE1-ORF1p/ SOX2, and TP53/SOX2 immunofluorescence staining were acquired using the 60×1.2 objective on Nikon A1R, running NIS Elements acquisition software. Three SOX2⁺ images were taken near the ventricular zone for each replicate of the prenatal human euploid and DS brains, with three replicates per slide. SOX2⁺ cells were selected using Imaris software (RRID:SCR_007370) based on an arbitrary intensity threshold and assessed for nuclear LMNB1 and TP53 colocalization within the imaged plane. The average nuclear LMNB1 and TP53 intensities were calculated for each plane and then averaged across replicates. Background subtraction was performed using the ImageJ software (RRID:SCR_003070) prior to calculating the average intensities of LINE-ORF1 for each plane and averaged across replicates.

Epifluorescence Imaging and fluorescence intensity quantification

Epifluorescence images of ROBO1/NEUN were acquired using the 20x objective on a Zeiss Axio Imager.M2 upright microscope. For each replicate, three images were acquired in the neocortex, resulting in a total of nine images per sample. All imaging was captured using the Zen Blue software (Carl Zeiss Meditec, v3.3.89.0000). NEUN⁺ cells were selected using Imaris software (RRID:SCR_007370) based on an arbitrary intensity threshold and assessed for nuclear ROBO1 colocalization within the imaged plane. The average nuclear ROBO1 intensities were calculated for each plane and then averaged across replicates.

Proteomics Sample Preparation

Prenatal human brain tissue was lysed in 500 μL of 5% SDS, 50 mM TEAB (Supplementary Data 1). Samples were sonicated at 30%

amplitude for 15 sec (5 sec on, 3 sec off for three cycles) with 1/8" micropipet, then resuspended with a pipette. Because of DNA, 1 μL (250U) of TurboNuclease was added to each sample, and they were sonicated again. To ensure proper lysis, samples were resuspended with a pipette and centrifuged at 16,000xg for 5 min. Supernatant was moved to a new tube, and the BCA protein concentration assay was performed. 10 μg of protein material (in 5% SDS, 50 mM TEAB) was reduced at 20 mM DTT for 10 min at 95 °C and alkylated with 40 mM iodoacetamide for 30 min in the dark. Samples were brought up to final concentration of 5% SDS and phosphoric acid was added to a final concentration of 1.2%. 165 μL of S-Trap protein binding buffer (90% methanol, 100 mM TEAB) was added to 27.5 μL of acidified lysate. Resulting mixture was passed through the micro column at 4000xg. The micro-column was washed 4 times with the S-Trap protein binding buffer. Each sample was digested with 1 μL of trypsin (in 20 μL of 50 mM TEAB) for 1 hr at 47 °C. Prior to elution, 40 μL of 50 mM TEAB pH 8 was added to the column. Peptides were eluted by centrifugation at 4000 xg. Peptides were eluted 2 more times with 40 μL 0.2% formic acid and 40 μL of 50% acetonitrile + 0.2% formic acid. Eluted peptides were dried down and stored at -40 °C. Control 2 was excluded from analysis due to significant variability.

Liquid chromatography-mass spectrometry

For data-independent acquisition (DIA) LC-MS/MS, 100 ng of the digested peptides were analyzed using a nano-HPLC (high-performance liquid chromatography) couple to MS. Samples were separated on an Aurora Elite TS column (IonOpticks Pty Ltd.). The sample in 5% formic acid was trap (300 μm i.d., 0.5 cm length, product#: 174500) loaded at 800 bar, onto a 75 μm i.d.x 15 cm nano-spray emitter (packed with 1.7 μm C18 beads) heated at 50 °C with the TS Interface. Peptides were eluted from the column with an acetonitrile gradient generated by a Vanquish Neo UHPLC System (Thermo Fisher Scientific Inc.) and analyzed on an Orbitrap™ Astral™. The gradient was delivered at 600 nL/min from 0.8% acetonitrile with 0.1% formic acid to 6.4% acetonitrile with 0.1% formic acid over 1 minute, 6.4% to 35.2% acetonitrile with 0.1% formic acid over 10 min. This was followed by a column wash of 76% acetonitrile with 0.1% formic acid over 4 min. The total DIA protocol is 15 min. Advanced peak determination was turned on with an expected LC peak width of 6 s. FAIMS was used with one compensation voltage at -50V. MS1 scan was from 380-980 m/z with an orbitrap resolution of 240,000. Normalized AGC target of 500%, and 10 ms maximum injection time in profile mode. DIA windows were set to auto with 2 m/z window sizes with 0 overlap, in the precursor range of 380-980 m/z. HCD collision energy was set to 25% using the Astral detector. The scan range was 150-2000 m/z with RF lens set to 40%, AGC target to 500%, and maximum injection time of 3 ms.

Mass spectrometry data analysis

Spectronaut v18.7 directDIA+ workflow with BGS Factory settings was used to search the raw data¹⁰¹ with the Spectronaut generated human spectral library (Human_PDB_2023). The FASTA database used is the Uniprot UP000005640 reviewed human database with contaminants (<https://www.ncbi.nlm.nih.gov/pmc/articles/PMC1004025/>). Parameters for the search were default. Run-wise imputing was turned on with global normalization. The differential abundance testing used was the unpaired t-test.

Microenvironment analysis

This custom analysis aimed to quantify changes in local cell type compositions between DS and euploid in the Slide-seq and MERFISH datasets. For each cell type A (center cell), we identified its closest Ntotal neighboring cells based on spatial coordinates obtained from the spatial transcriptomics data. We calculated the B ratio, which represents the proportion of a specific cell type B (query cell) within these top Ntotal neighboring cells of cell type A, where N_B is the

number of neighboring cells of type B within the N_{total} nearest neighbors of cell i of type A. In our analysis, we set $N_{total} = 100$ to capture the immediate cellular microenvironment around each cell. This B ratio allows us to detect whether the local environment of a specific cell type B is enriched or depleted around another cell type A in the DS brain compared to euploid. An increased B ratio in DS indicates a higher local density of cell type B around cell type A.

We used the Wilcoxon rank-sum test to assess differences in B ratio distributions between DS and euploid for each cell pair (A-B). A Linear Mixed-Effects Model was applied to account for inter-sample variability, with the B ratio log-transformed for normality. The models were:

Full Model:

$$Y = \beta_0 + \beta \cdot X + \mu_{sample} + \epsilon$$

Reduced Model:

$$Y = \beta_0 + \mu_{sample} + \epsilon$$

Where, Y is the log(B ratio); $\beta \cdot X$ represents the fixed effect of Conditions, where β is the coefficient of Conditions, and X represents the Conditions predictor. μ_{sample} is the random effect for Sample. ϵ is the residual error term.

We used a likelihood ratio test to compare the models and evaluate the significance of the DS condition on B ratio changes. Significant alterations in the cellular microenvironment were determined based on effect size (positive effect size indicates increased clustering in DS) and p-values, with a threshold of 0.05 after multiple comparisons correction using the BH procedure.

In the LOSO approach, the microenvironment code was iteratively executed, leaving one sample out each time. The mean and standard deviation for each iteration were calculated and plotted to identify conserved or divergent effect sizes, both positive and negative.

Mouse model of Down syndrome

Ts65Dn (*B6EiC3Sn.BLiA-Ts(1716)65Dn/Dnj*, RRID:IMSR_JAX:005252) and euploid controls (*B6EiC3Sn.BLiAF1/J*, RRID:IMSR_JAX:003647) were procured from Jackson Laboratories. Mice were maintained in 12 hr light-dark cycles, with an ambient temperature of 20-22 °C and 40-55% humidity. Mice had free access to chow and food at the Centre for Phenogenomics in Toronto, ON, Canada. All animal experiments were carried out in accordance with the Canadian Council of Animal Care policies. For breeding purposes, Ts65Dn mice were paired with euploid controls as per the recommendations provided by Jackson Laboratories. At both postnatal and 6-month time points, three mice (female and male) per condition were utilized for MERFISH studies. Fresh brain tissue was promptly collected, embedded in OCT solution, and stored at -80 °C until MERFISH processing.

Gene panel design for MERFISH

To investigate the neurodevelopmental and mature characteristics of the DS brain with spatial awareness, a meticulously chosen panel of 500 genes was used for MERFISH analysis (Supplementary Data 7). Among these, 132 genes served as canonical markers for identifying various cell types, encompassing ExN and InN, as well as glial cells such as astrocytes, microglia, and OLs. Additionally, non-neuronal cell types including fibroblasts, ependymal cells, and vascular cells were also represented in this gene panel for comprehensive cellular identification. The remaining genes in the panel encompassed biologically relevant signaling pathways (WNT, JAK/STAT, MAPK), ligand-receptor interactions, inflammatory markers, senescence-associated signatures, and extracellular matrix components related to DS.

Tissue processing and sample preparation for MERFISH

Brain tissue was harvested from P0 and 6mo mice that were euthanized using CO₂, immediately embedded using optimal cutting temperature (OCT) compound, and stored in -80 °C during short-term storage. Frozen-embedded samples were cryo-sectioned at -20 °C at 10 µm thickness prior to mounting on MERSCOPE beaded coverslips (Vizgen, Cat: 10500001). Following, tissue sections were refrozen for 5-15 min, fixed with 4% paraformaldehyde (PFA) diluted in 1X PBS for 15 min, washed three times with 1X PBS for 5 min each, and stored in 70% ethanol at 4 °C to allow for tissue permeabilization. Sections were stored in 70% ethanol for no longer than 3 weeks until all imaging from animals of the same age was completed. Sample preparation, including probe hybridization and gel embedding, was performed using Vizgen's sample preparation kit (Vizgen, Cat: 10400012) as detailed in Vizgen's manufacturer's instructions for unfixed tissue. Following, samples were washed twice with Sample Prep Wash Buffer, incubated with DAPI and Poly-T Staining Reagent (Vizgen, PN 20300021) for 15 min on a rocker, washed with Formamide Wash Buffer for 10 min, and washed once more with Sample Prep Wash Buffer.

MERFISH imaging

Each section was imaged on the MERSCOPE platform (Vizgen, Cat: 10000001) using the MERSCOPE 500 Gene Imaging Kit, as detailed according to the manufacturer's instructions. Samples were placed into the flow chamber and carefully connected to the fluidics of the MERSCOPE machine to avoid air bubbles. A low-resolution mosaic of DAPI and Poly-T stains were used to identify the region of interest for imaging. Seven 1.5 µm thick z planes were taken to capture the entire 10 µm thickness of the tissue sections with high-resolution imaging. Imaging was performed automatically using the MERSCOPE imaging presets.

MERFISH Bioinformatic Pipeline

MERFISH images were segmented using Vizgen's post-processing tool (VPT) and Cellpose, a machine learning algorithm (RRID:SCR_021716)¹⁰¹. DAPI and polyT signals were used to delineate cell boundaries for each field-of-view. Individual RNA molecules were assigned to a cell based on whether they were positioned within a marked boundary. Fluorescence intensity was summed and quantified in a cell-by-gene matrix (where rows and columns represented cell and gene identification, respectively). Anatomical segmentation of the P0 and 6mo brains revealed 8 gross anatomical regions: superficial cortex layers, deeper cortex layers, corpus callosum, subventricular zones, caudoputamen, lateral septal nucleus, anterior commissure, lower gray matter. The cortex, corpus callosum, and subventricular zone were chosen for analysis due to their relevance in higher executive functioning and neurogenesis.

Adapted from an existing bioinformatic pipeline¹⁰², the cell-by-gene matrix of each replicate was processed as follows. (1) Despite properly segmenting cells on DAPI-oversaturated images, Watershed segmentation posed a problem with a small fraction of cells, with very small and very large volumes, which were still generated using VPT and Cellpose. A volume filtration was performed on cells with a volume less than 50 µm³ or larger than three times the median volume of all cells. (2) Cells with zero RNA molecules were removed. (3) In a 10 µm³ thick tissue slice, the spatial orientation of cells within the section resulted in partial imaging of their soma. To account for potential RNA discrepancies, gene expression for each cell was normalized by their volume and multiplied by 1000. (4) A variability in the mean total transcripts was observed for each sample. A scaling factor was applied to adjust the raw RNA counts to the mean number of RNA transcripts between samples to equalize the average expression level within the dataset. (5) Cells with RNA counts falling below 2% quantile or exceeding the 98% quantile were removed. (6) Potential doublets were removed using Scrublet¹⁰³, a Python-based program that generates artificial doublets by comparing gene expression profiles of randomly

selecting cells with segmented cells in the dataset and using a k-nearest neighbor (kNN) to output a predicted doublet score.

MERFISH granular cell type identification

Integrative clustering analysis of the cortex, subventricular zone, and corpus callosum MERFISH single-cell transcriptome profiles was performed on 98,418 cells, 20,608 cells, and 2380 cells in the P0 dataset and 108,591 cells, 2562 cells, and 8365 cells in the 6mo dataset using Seurat v5 (RRID:SCR_016341). Clusters expressing two or more mutually exclusive canonical cell markers, likely representative of doublets, were removed. Neuronal cell types were removed from the corpus callosum datasets.

Re-clustering of P0 cortical ExN revealed seven subtypes of layer-specific ExN, including clusters spatially concentrated in cortical layers II-III and expressing elevated levels of *Cux2*, *Mef2c*, and *Satb2* (L2-3 ExN); clusters spatially concentrated in cortical layers II-IV and expressing moderate levels of *Cux2*, *Mef2c*, and *Satb2* (L2-4 ExN); clusters spatially concentrated in cortical layers II-V and expressing moderate levels of *Cux2* and *Mef2c* and high levels of *Otx1* (L2-5 ExN); clusters spatially concentrated in cortical layers V-VIa expressing high levels of *Tle4* and *Ccn2* (L5-6a ExN); clusters spatially concentrated in layer VIb expressing high levels of *Ccn2* (L6b ExN); one cluster of cells spatially concentrated in the subplate expressing high levels of *Nr4a2*; two clusters of cells spatially concentrated in the piriform cortex defined based on the absence (*Piri 1* ExN) or presence of *Fabp7* and *Ascl1* (*Piri 2* ExN). Reclustering of the 6mo cortical ExN revealed 5 additional layer-specific ExN, including clusters spatially concentrated in cortical layer I and expressing elevated levels of *Tle1*, *Rgs8*, and *Cux2* (L1 ExN); clusters spatially concentrated in layers IV-V (L4-5 ExN) and layers IV-VIa (L4-6a ExN) expressing moderate levels of *Cux*, *Mef2c*, and *Tle4*; clusters spanning cortical layers I-VIa (L1-6a ExN) and layers II-VIa (L2-6a ExN) expressing *Otx1*, *Tle4*, and *Ccn2* (Supplementary Fig. 5a-f).

Re-clustering of InN in the P0 and 6mo datasets revealed three subtypes present in the cortex and subventricular zone (InN 1-3), including general InN expressing *Gad1* (InN1), *Sst*, *Lhx6*, and *Arx*-expressing InN (InN2), and *Vip* and *Cnr1*-expressing InN (InN 3). Re-clustering of TAPs revealed two subtypes, which were distinguished based on low (TAPs 1) or moderate (TAPs 2) *Gad1* and *Gad2* expression. Interestingly, NSCs were distinguished by their distinct spatial organizations along the subventricular zone, and were annotated as follows: NSCs 1, representing NSCs dispersed across the lateral, dorsal, medial, and septal walls; NSCs 2, characterized by spatial concentration near the lateral wall and elevated *Crym* expression; NSCs 3, concentrated near the dorsal wall; and NSCs 4, concentrated near the medial wall (Supplementary Fig. 5a-f).

In the P0 and 6mo datasets, we found three subtypes of astrocytes: proliferating immature astrocytes (Astro 1) were annotated based on *Vcam1*, *Aldh1l1*, *Fabp7*, and *Mki67* expression; immature astrocytes were annotated using the same markers but lacked *Mki67* expression (Astro 2); mature astrocytes were annotated using *Aqp4*, *Gfap*, and *C4b* (Astro 3). Interestingly, a distinct astrocytic cluster exhibited exclusive expression of *Gfap* and displayed spatial concentration near the meninges of the 6mo cortex—likely representative of perivascular astrocytes near meninges (Astro 4). Re-clustering of immune cells revealed two subtypes of microglia, with one homeostatic population expressing *Cx3cr1*, *Trem2*, and *Csf1r* (Micro 1), and a second population expressing elevated phagocytic markers *Aif1* and *Cd68* (Micro 2). A third class within the immune cell population, devoid of specific microglia, macrophage, and monocyte markers, and solely expressing *Csf1r*, was likely representative of myeloid progenitor cells (Myeloid). Re-clustering of vascular cells revealed two subtypes, with one population expressing endothelial markers *Pecam1* and *Esam* (SM 2) and a second population expressing high pericyte *Kcnj8* and *Atp13a5* markers in addition to endothelial markers (SM1). Re-clustering of OPC revealed two subtypes, including a population (OPC 1) expressing

elevated *Pdgfra*, *Sox10*, and *Olig1*, and a second population expressing moderate *Pdgfra* and *Sox10*, but with reduced *Olig1* expression (OPC 2) (Supplementary Fig. 5a-f).

Reporting summary

Further information on research design is available in the Nature Portfolio Reporting Summary linked to this article.

Data availability

Raw files for human single-nucleus sequencing, Slide-seq, and MERFISH have been deposited in GEO under the accession codes GSE280175, GSE280170, and GSE280177, respectively. Proteomics data has been deposited as a complete submission to the MassIVE repository (<https://massive.ucsd.edu/ProteoSAFe/static/massive.jsp>) and assigned the accession number MSV000096108. Source data are provided with this paper.

Code availability

Custom code used for the microenvironment analysis, along with additional relevant scripts from this manuscript is available on Github at <https://github.com/annaminyifeng/Molecular-Cartography-of-DS-Brain>. Reproducible results for the microenvironment analysis can also be accessed via Code Ocean at <https://doi.org/10.24433/CO.4591687.v2>. Open-source algorithms were used as detailed for the snRNA-seq, Slide-seq, and MERFISH analyses.

References

1. Antonarakis, S. E. et al. Down syndrome. *Nat. Rev. Dis. Prim.* **6**, 9 (2020).
2. Lott, I. T. & Head, E. Dementia in down syndrome: Unique insights for alzheimer disease research. *Nat. Rev. Neurol.* **15**, 135–147 (2019).
3. Schmidt-Sidor, B., Wisniewski, K. E., Shepard, T. H. & Sersen, E. A. Brain growth in down syndrome subjects 15 to 22 weeks of gestational age and birth to 60 months. *Clin. Neuropathol.* **9**, 181–190 (1990).
4. Wisniewski, K. E. Down syndrome children often have brain with maturation delay, retardation of growth, and cortical dysgenesis. *Am. J. Med. Genet. Suppl.* **7**, 274–281 (1990).
5. Murray, A. et al. Brief report: isogenic induced pluripotent stem cell lines from an adult with mosaic down syndrome model accelerated neuronal ageing and neurodegeneration. *Stem Cells Dayt. Ohio* **33**, 2077–2084 (2015).
6. Stagni, F., Giacomini, A., Emili, M., Guidi, S. & Bartesaghi, R. Neurogenesis impairment: An early developmental defect in Down syndrome. *Free Radic. Biol. Med.* **114**, 15–32 (2018).
7. Guidi, S. et al. Neurogenesis impairment and increased cell death reduce total neuron number in the hippocampal region of fetuses with Down syndrome. *Brain Pathol. Zur. Switz.* **18**, 180–197 (2008).
8. Haydar, T. F. & Reeves, R. H. Trisomy 21 and early brain development. *Trends Neurosci.* **35**, 81–91 (2012).
9. Lu, J. et al. OLIG2 over-expression impairs proliferation of human Down syndrome neural progenitors. *Hum. Mol. Genet.* **21**, 2330–2340 (2012).
10. Ponroy Bally, B. & Murai, K. K. Astrocytes in down syndrome across the lifespan. *Front. Cell. Neurosci.* **15**, 702685 (2021).
11. Pinter, J. D., Eliez, S., Schmitt, J. E., Capone, G. T. & Reiss, A. L. Neuroanatomy of down's syndrome: a high-resolution MRI study. *Am. J. Psychiatry* **158**, 1659–1665 (2001).
12. Carducci, F. et al. Whole-brain voxel-based morphometry study of children and adolescents with Down syndrome. *Funct. Neurol.* **28**, 19–28 (2013).
13. Stickels, R. R. et al. Highly sensitive spatial transcriptomics at near-cellular resolution with Slide-seqV2. *Nat. Biotechnol.* **39**, 313–319 (2021).

14. Moffitt, J. R. et al. High-throughput single-cell gene-expression profiling with multiplexed error-robust fluorescence in situ hybridization. *Proc. Natl Acad. Sci. USA.* **113**, 11046–11051 (2016).
15. Chen, K. H., Boettiger, A. N., Moffitt, J. R., Wang, S. & Zhuang, X. RNA imaging. Spatially resolved, highly multiplexed RNA profiling in single cells. *Science* **348**, aaa6090 (2015).
16. Xu, C. et al. Automatic cell-type harmonization and integration across Human Cell Atlas datasets. *Cell* **186**, 5876–5891.e20 (2023).
17. Andrews, M. G. et al. LIF signaling regulates outer radial glial to interneuron fate during human cortical development. *Cell Stem Cell* **30**, 1382–1391.e5 (2023).
18. Liu, D. D. et al. Purification and characterization of human neural stem and progenitor cells. *Cell* **186**, 1179–1194.e15 (2023).
19. Pollen, A. A. et al. Low-coverage single-cell mRNA sequencing reveals cellular heterogeneity and activated signaling pathways in developing cerebral cortex. *Nat. Biotechnol.* **32**, 1053–1058 (2014).
20. Pebworth, M.-P., Ross, J., Andrews, M., Bhaduri, A. & Kriegstein, A. R. Human intermediate progenitor diversity during cortical development. *Proc. Natl Acad. Sci. USA.* **118**, e2019415118 (2021).
21. Hansen, D. V. et al. Non-epithelial stem cells and cortical interneuron production in the human ganglionic eminences. *Nat. Neurosci.* **16**, 1576–1587 (2013).
22. Wang, L. et al. Molecular and cellular dynamics of the developing human neocortex. *Nature* <https://doi.org/10.1038/s41586-024-08351-7> (2025).
23. Velmeshov, D. et al. Single-cell analysis of prenatal and postnatal human cortical development. *Science* **382**, eadf0834 (2023).
24. Park, S. H. E., Kulkarni, A. & Konopka, G. FOXP1 orchestrates neurogenesis in human cortical basal radial glial cells. *PLoS Biol.* **21**, e3001852 (2023).
25. Hevner, R. F. Layer-specific markers as probes for neuron type identity in human neocortex and malformations of cortical development. *J. Neuropathol. Exp. Neurol.* **66**, 101–109 (2007).
26. Torres-Berrio, A., Hernandez, G., Nestler, E. J. & Flores, C. The Netrin-1/DCC Guidance Cue Pathway as a Molecular Target in Depression: Translational Evidence. *Biol. Psychiatry* **88**, 611–624 (2020).
27. Miyoshi, G. & Fishell, G. Dynamic FoxG1 expression coordinates the integration of multipolar pyramidal neuron precursors into the cortical plate. *Neuron* **74**, 1045–1058 (2012).
28. Zeng, H. et al. Large-scale cellular-resolution gene profiling in human neocortex reveals species-specific molecular signatures. *Cell* **149**, 483–496 (2012).
29. Faedo, A. et al. Differentiation of human telencephalic progenitor cells into MSNs by inducible expression of Gsx2 and Ebf1. *Proc. Natl Acad. Sci. USA.* **114**, E1234–E1242 (2017).
30. Precious, S. V. et al. FoxP1 marks medium spiny neurons from precursors to maturity and is required for their differentiation. *Exp. Neurol.* **282**, 9–18 (2016).
31. Garma, L. D. et al. Interneuron diversity in the human dorsal striatum. *Nat. Commun.* **15**, 6164 (2024).
32. Conforti, P. et al. In vitro-derived medium spiny neurons recapitulate human striatal development and complexity at single-cell resolution. *Cell Rep. Methods* **2**, 100367 (2022).
33. He, J. et al. Transcriptional and anatomical diversity of medium spiny neurons in the primate striatum. *Curr. Biol. CB* **31**, 5473–5486.e6 (2021).
34. Araujo, D. J. et al. FoxP1 orchestration of ASD-relevant signaling pathways in the striatum. *Genes Dev.* **29**, 2081–2096 (2015).
35. Rastogi, M. et al. Integrative multi-omic analysis reveals conserved cell-projection deficits in human Down syndrome brains. *Neuron* **112**, 2503–2523.e10 (2024).
36. Cable, D. M. et al. Robust decomposition of cell type mixtures in spatial transcriptomics. *Nat. Biotechnol.* **40**, 517–526 (2022).
37. Ait Yahya-Graison, E. et al. Classification of human chromosome 21 gene-expression variations in Down syndrome: impact on disease phenotypes. *Am. J. Hum. Genet.* **81**, 475–491 (2007).
38. Stamoulis, G. et al. Single cell transcriptome in aneuploidies reveals mechanisms of gene dosage imbalance. *Nat. Commun.* **10**, 4495 (2019).
39. Olmos-Serrano, J. L. et al. Down Syndrome Developmental Brain Transcriptome Reveals Defective Oligodendrocyte Differentiation and Myelination. *Neuron* **89**, 1208–1222 (2016).
40. Li, C.-M. et al. Cell type-specific over-expression of chromosome 21 genes in fibroblasts and fetal hearts with trisomy 21. *BMC Med. Genet.* **7**, 24 (2006).
41. Finak, G. et al. MAST: a flexible statistical framework for assessing transcriptional changes and characterizing heterogeneity in single-cell RNA sequencing data. *Genome Biol.* **16**, 278 (2015).
42. Gene Ontology Consortium et al. The Gene Ontology knowledgebase in 2023. *Genetics* **224**, iyad031 (2023).
43. Ashburner, M. et al. Gene ontology: tool for the unification of biology. The Gene Ontology Consortium. *Nat. Genet.* **25**, 25–29 (2000).
44. Milacic, M. et al. The reactome pathway knowledgebase 2024. *Nucleic Acids Res* **52**, D672–D678 (2024).
45. Gonda, Y., Namba, T. & Hanashima, C. Beyond axon guidance: Roles of slit-robo signaling in neocortical formation. *Front. Cell Dev. Biol.* **8**, 607415 (2020).
46. Meharena, H. S. et al. Down-syndrome-induced senescence disrupts the nuclear architecture of neural progenitors. *Cell Stem Cell* **29**, 116–130.e7 (2022).
47. Contestabile, A., Magara, S. & Cancedda, L. The GABAergic hypothesis for cognitive disabilities in down syndrome. *Front. Cell. Neurosci.* **11**, 54 (2017).
48. Deidda, G. et al. Reversing excitatory GABAAR signaling restores synaptic plasticity and memory in a mouse model of Down syndrome. *Nat. Med.* **21**, 318–326 (2015).
49. Pollen, A. A. et al. Molecular identity of human outer radial glia during cortical development. *Cell* **163**, 55–67 (2015).
50. Bergen, V., Lange, M., Peidli, S., Wolf, F. A. & Theis, F. J. Generalizing RNA velocity to transient cell states through dynamical modeling. *Nat. Biotechnol.* **38**, 1408–1414 (2020).
51. Svensson, V. & Pachter, L. RNA Velocity: Molecular kinetics from single-cell RNA-Seq. *Mol. Cell* **72**, 7–9 (2018).
52. Liu, Y. et al. Systematic proteome and proteostasis profiling in human Trisomy 21 fibroblast cells. *Nat. Commun.* **8**, 1212 (2017).
53. Li, W. et al. Activation of transposable elements during aging and neuronal decline in Drosophila. *Nat. Neurosci.* **16**, 529–531 (2013).
54. Belancio, V. P., Roy-Engel, A. M. & Deininger, P. L. All y'all need to know'bout retroelements in cancer. *Semin. Cancer Biol.* **20**, 200–210 (2010).
55. Rodríguez-Quiroz, R. & Valdebenito-Maturana, B. SoloTE for improved analysis of transposable elements in single-cell RNA-Seq data using locus-specific expression. *Commun. Biol.* **5**, 1063 (2022).
56. Reeves, R. H. et al. A mouse model for down syndrome exhibits learning and behaviour deficits. *Nat. Genet.* **11**, 177–184 (1995).
57. Sunkin, S. M. et al. Allen Brain Atlas: an integrated spatio-temporal portal for exploring the central nervous system. *Nucleic Acids Res* **41**, D996–D1008 (2013).
58. Matsumata, M. et al. The effects of Fabp7 and Fabp5 on postnatal hippocampal neurogenesis in the mouse. *Stem Cells Dayt. Ohio* **30**, 1532–1543 (2012).
59. Rieskamp, J. D. et al. Excitatory amino acid transporter 1 supports adult hippocampal neural stem cell self-renewal. *iScience* **26**, 107068 (2023).

60. Chakrabarti, L. et al. Olig1 and Olig2 triplication causes developmental brain defects in Down syndrome. *Nat. Neurosci.* **13**, 927–934 (2010).
61. Stagni, F. & Bartesaghi, R. The challenging pathway of treatment for neurogenesis impairment in down syndrome: Achievements and perspectives. *Front. Cell. Neurosci.* **16**, 903729 (2022).
62. Gupta, M., Dhanasekaran, A. R. & Gardiner, K. J. Mouse models of down syndrome: gene content and consequences. *Mamm. Genome. J. Int. Mamm. Genome Soc.* **27**, 538–555 (2016).
63. Rusu, B. et al. Single-nucleus profiling identifies accelerated oligodendrocyte precursor cell senescence in a mouse model of down syndrome. *eNeuro* **10**, ENEURO.0147–23.2023 (2023).
64. Laan, L. et al. DNA methylation changes in Down syndrome derived neural iPSCs uncover co-dysregulation of ZNF and HOX3 families of transcription factors. *Clin. Epigenetics* **12**, 9 (2020).
65. Criscione, S. W., Teo, Y. V. & Neretti, N. The chromatin landscape of cellular senescence. *Trends Genet. TIG* **32**, 751–761 (2016).
66. Ito, T., Teo, Y. V., Evans, S. A., Neretti, N. & Sedivy, J. M. Regulation of cellular senescence by polycomb chromatin modifiers through distinct DNA damage- and histone methylation-dependent pathways. *Cell Rep.* **22**, 3480–3492 (2018).
67. Herr, L. M., Schaffer, E. D., Fuchs, K. F., Datta, A. & Brosh, R. M. Replication stress as a driver of cellular senescence and aging. *Commun. Biol.* **7**, 616 (2024).
68. Wu, W. et al. Directional guidance of neuronal migration in the olfactory system by the protein Slit. *Nature* **400**, 331–336 (1999).
69. Krivega, M. et al. Genotoxic stress in constitutive trisomies induces autophagy and the innate immune response via the cGAS-STING pathway. *Commun. Biol.* **4**, 831 (2021).
70. Galbraith, M. D. et al. Multidimensional definition of the interferonopathy of Down syndrome and its response to JAK inhibition. *Sci. Adv.* **9**, eadg6218 (2023).
71. Zhu, P. J. et al. Activation of the ISR mediates the behavioral and neurophysiological abnormalities in Down syndrome. *Science* **366**, 843–849 (2019).
72. Dunkelberger, J. R. & Song, W.-C. Complement and its role in innate and adaptive immune responses. *Cell Res.* **20**, 34–50 (2010).
73. Gibson, B., Goodfriend, E., Zhong, Y. & Melhem, N. M. Fetal inflammatory response and risk for psychiatric disorders. *Transl. Psychiatry* **13**, 224 (2023).
74. Magdalou, J. et al. Complement system in brain architecture and neurodevelopmental disorders. *Front. Neurosci.* **14**, 23 (2020).
75. Gorelik, A. et al. Developmental activities of the complement pathway in migrating neurons. *Nat. Commun.* **8**, 15096 (2017).
76. Toda, T. et al. Long interspersed nuclear elements safeguard neural progenitors from precocious differentiation. *Cell Rep.* **43**, 113774 (2024).
77. Gebrie, A. Transposable elements as essential elements in the control of gene expression. *Mob. DNA* **14**, 9 (2023).
78. Mangoni, D. et al. LINE-1 regulates cortical development by acting as long non-coding RNAs. *Nat. Commun.* **14**, 4974 (2023).
79. Fort, V., Khelifi, G. & Hussein, S. M. I. Long non-coding RNAs and transposable elements: A functional relationship. *Biochim. Biophys. Acta Mol. Cell Res.* **1868**, 118837 (2021).
80. Horn, A. V., Celic, I., Dong, C., Martirosyan, I. & Han, J. S. A conserved role for the ESCRT membrane budding complex in LINE retrotransposition. *PLoS Genet.* **13**, e1006837 (2017).
81. Di Stefano, L. All Quiet on the TE Front? The role of chromatin in transposable element silencing. *Cells* **11**, 2501 (2022).
82. Pappalardo, X. G. & Barra, V. Losing DNA methylation at repetitive elements and breaking bad. *Epigenetics Chromatin* **14**, 25 (2021).
83. Chakrabarti, L., Galdzicki, Z. & Haydar, T. F. Defects in embryonic neurogenesis and initial synapse formation in the forebrain of the Ts65Dn mouse model of Down syndrome. *J. Neurosci. J. Soc. Neurosci.* **27**, 11483–11495 (2007).
84. Contestabile, A. et al. Cell cycle alteration and decreased cell proliferation in the hippocampal dentate gyrus and in the neocortical germinal matrix of fetuses with Down syndrome and in Ts65Dn mice. *Hippocampus* **17**, 665–678 (2007).
85. Lockrow, J. P., Fortress, A. M. & Granholm, A.-C. E. Age-related neurodegeneration and memory loss in down syndrome. *Curr. Gerontol. Geriatr. Res.* **2012**, 463909 (2012).
86. Stringer, C. A. et al. Aquaporin-4: Unraveling the link between reactive astrogliosis and neuroinflammation in down syndrome with alzheimer's disease pathogenesis. *Alzheimers Dement* **20**, e092708 (2025).
87. Williams, C. G., Lee, H. J., Asatsuma, T., Vento-Tormo, R. & Haque, A. An introduction to spatial transcriptomics for biomedical research. *Genome Med* **14**, 68 (2022).
88. Petukhov, V. et al. Cell segmentation in imaging-based spatial transcriptomics. *Nat. Biotechnol.* **40**, 345–354 (2022).
89. Herault, Y. et al. Rodent models in down syndrome research: impact and future opportunities. *Dis. Model. Mech.* **10**, 1165–1186 (2017).
90. Rueda, N., Flórez, J. & Martínez-Cué, C. Mouse models of down syndrome as a tool to unravel the causes of mental disabilities. *Neural Plast.* **2012**, 584071 (2012).
91. Martinez de Lagran, M., Elizalde-Torrent, A., Paredes, R., Clotet, B. & Dierssen, M. Lamivudine, a reverse transcriptase inhibitor, rescues cognitive deficits in a mouse model of down syndrome. *J. Cell. Mol. Med.* **26**, 4210–4215 (2022).
92. Duchon, A. et al. Ts66Yah, a mouse model of down syndrome with improved construct and face validity. *Dis. Model. Mech.* **15**, dmm049721 (2022).
93. Braun, E. et al. Comprehensive cell atlas of the first-trimester developing human brain. *Science* **382**, eadf1226 (2023).
94. Yao, Z. et al. A high-resolution transcriptomic and spatial atlas of cell types in the whole mouse brain. *Nature* **624**, 317–332 (2023).
95. Domínguez Conde, C. et al. Cross-tissue immune cell analysis reveals tissue-specific features in humans. *Science* **376**, eabl5197 (2022).
96. Biancalani, T. et al. Deep learning and alignment of spatially resolved single-cell transcriptomes with Tangram. *Nat. Methods* **18**, 1352–1362 (2021).
97. Hao, Y. et al. Dictionary learning for integrative, multimodal and scalable single-cell analysis. *Nat. Biotechnol.* **42**, 293–304 (2024).
98. La Manno, G. et al. RNA velocity of single cells. *Nature* **560**, 494–498 (2018).
99. Wheeler, T. J. et al. Dfam: a database of repetitive DNA based on profile hidden Markov models. *Nucleic Acids Res.* **41**, D70–D82 (2013).
100. Bao, W., Kojima, K. K. & Kohany, O. Repbase update, a database of repetitive elements in eukaryotic genomes. *Mob. DNA* **6**, 11 (2015).
101. Pachitariu, M. & Stringer, C. Cellpose 2.0: how to train your own model. *Nat. Methods* **19**, 1634–1641 (2022).
102. Zhang, M. et al. Spatially resolved cell atlas of the mouse primary motor cortex by MERFISH. *Nature* **598**, 137–143 (2021).
103. Wolock, S. L., Lopez, R. & Klein, A. M. Scrublet: Computational identification of cell doublets in single-cell transcriptomic data. *Cell Syst.* **8**, 281–291.e9 (2019).

Acknowledgements

We would like to thank Dr. Kimberly Lau and Dr. Paul Paroutis at the SickKids Imaging Facility for their assistance with the confocal imaging and image analysis. We would also like to thank Cassandra Wong and Brendon Seale of the Network Biology Collaborative Centre Proteomics Facility (RRID: SCR_025375) at the Lunenfeld-Tanenbaum Research Institute for global proteome analysis. The facility is supported by the Canada Foundation for Innovation and the Ontario Government. This

work was supported by research funds from the Hospital for Sick Children to B.T.K; M. Y. F is a recipient of the Canadian Institutes of Health Research and Ontario Graduate Scholarship.

Author contributions

Overall conceptualization, B.T.K. snRNA-seq and Slide-seq sample preparation, data generation, and analysis, M.Y.F., W.C., G.L., B.K., and B.T.K. MERFISH sample preparation, data generation, and analysis, M.Y.F., W.C., G.L., B.K., N.T., B.R., and B.T.K. Proteomics sample preparation, M.Y.F., J.Y.Y., and B.T.K. Manuscript writing, M.Y.F. and B.T.K. All authors edited the final manuscript.

Competing interests

The authors declare no competing interests.

Additional information

Supplementary information The online version contains supplementary material available at
<https://doi.org/10.1038/s41467-025-63752-0>.

Correspondence and requests for materials should be addressed to Brian T. Kalish.

Peer review information *Nature Communications* thanks William Mobley, and the other, anonymous, reviewer(s) for their contribution to the peer review of this work. A peer review file is available.

Reprints and permissions information is available at
<http://www.nature.com/reprints>

Publisher's note Springer Nature remains neutral with regard to jurisdictional claims in published maps and institutional affiliations.

Open Access This article is licensed under a Creative Commons Attribution-NonCommercial-NoDerivatives 4.0 International License, which permits any non-commercial use, sharing, distribution and reproduction in any medium or format, as long as you give appropriate credit to the original author(s) and the source, provide a link to the Creative Commons licence, and indicate if you modified the licensed material. You do not have permission under this licence to share adapted material derived from this article or parts of it. The images or other third party material in this article are included in the article's Creative Commons licence, unless indicated otherwise in a credit line to the material. If material is not included in the article's Creative Commons licence and your intended use is not permitted by statutory regulation or exceeds the permitted use, you will need to obtain permission directly from the copyright holder. To view a copy of this licence, visit <http://creativecommons.org/licenses/by-nc-nd/4.0/>.

© The Author(s) 2025